

## Article

# Sedimentary Characteristics and Depositional Model of the Paleogene Dawenkou Formation in Eastern China: Insights from the Huanggang Depression

Wentao Chen<sup>1,2</sup>, Dawei Lv<sup>1,3,\*</sup>, John I. Ejembi<sup>4</sup>, Bin Yang<sup>2</sup>, Cuiyu Song<sup>1,3</sup>, Zhenguo Ning<sup>2,\*</sup>, Lulu Tang<sup>2</sup>, Zhihui Zhang<sup>1,3</sup> and Haibo Jia<sup>1,3</sup>

<sup>1</sup> College of Earth Science and Engineering, Shandong University of Science and Technology, Qingdao 266590, China; chenwentao8618@163.com (W.C.); scy57273@126.com (C.S.); zhzhahui@sdust.edu.cn (Z.Z.); jiahaibohb@163.com (H.J.)

<sup>2</sup> Key Laboratory of Gold Mineralization Processes and Resource Utilization, Ministry of Natural Resources, Shandong Provincial Key Laboratory of Metallogenic Geological Process and Resource Utilization, Shandong Institute of Geological Sciences, Jinan 250013, China; yangbin71311@163.com (B.Y.); tanglulu@126.com (L.T.)

<sup>3</sup> Laboratory for Marine Mineral Resources, Qingdao National Laboratory for Marine Science and Technology, Qingdao 266071, China

<sup>4</sup> JiE Ventures, Houston, TX 77449, USA; jie@jievventures.com

\* Correspondence: lvdawei95@sdust.edu.cn (D.L.); ningzhenguodky@shandong.cn (Z.N.)

**Abstract:** The Huanggang depression in eastern China is a significant Cenozoic salt-bearing basin that formed during the alternating dry and wet climate periods from the Eocene to the Oligocene. Despite the economic importance of the Huanggang depression, its saliferous model remains controversial. To address this issue, we conducted comprehensive analyses of the sedimentology and elemental geochemistry on the YZR1 borehole core, which hosts a relatively complete sedimentary record of the Huanggang depression, consisting of five lithofacies' assemblages. The combined lithofacies and geochemical ratios, including B/Ga, Sr/Ba, and V/(V + Ni), provide insights into the paleolake's evolution in the Huanggang depression. Our analyses indicated that the paleolake underwent a transition from a freshwater lake to a brackish water/saline lake, subsequently transforming into a salt lake, reverting back to a brackish water/saline lake, and ultimately returning to its original state as a freshwater lake. These changes are reflected in the sedimentary record and inform the six stages of evolution of the paleolake of the Dawenkou Formation. We propose two metallogenic models to explain the accumulation of the thick halite (LA1) and thin halite layers (LA2), respectively. LA1 is primarily dominated by halite deposition, forming in an extremely shallow water environment under arid climate conditions. In contrast, LA2 records the alternating deposition of halite, anhydrite, and mudstone, and formed in a shallow water environment under arid to semi-arid climatic conditions. LA1 has a much drier climate and higher salinity than LA2. Our results suggest that the salt-forming period in the Huanggang depression occurred from the late Eocene to the early Oligocene. The halite in the Huanggang depression formed in a shallow water environment, providing the basis for the halite deposition model of the depression. This study sheds light on the formation mechanism of halite in the Paleogene in eastern China.

**Keywords:** petrography; major/trace elements; depositional and metallogenic model; Paleogene; Huanggang depression



**Citation:** Chen, W.; Lv, D.; Ejembi, J.I.; Yang, B.; Song, C.; Ning, Z.; Tang, L.; Zhang, Z.; Jia, H. Sedimentary Characteristics and Depositional Model of the Paleogene Dawenkou Formation in Eastern China: Insights from the Huanggang Depression. *Minerals* **2024**, *14*, 131. <https://doi.org/10.3390/min14020131>

Academic Editors: Yong Sik Gihm, Taejin Choi and Byung Choon Lee

Received: 7 January 2024

Revised: 22 January 2024

Accepted: 23 January 2024

Published: 25 January 2024



**Copyright:** © 2024 by the authors. Licensee MDPI, Basel, Switzerland. This article is an open access article distributed under the terms and conditions of the Creative Commons Attribution (CC BY) license (<https://creativecommons.org/licenses/by/4.0/>).

## 1. Introduction

Halite is a critical component of human life, but its metallogenic model has been the subject of ongoing debate. Prior to the 1960s, the traditional salt formation model was proposed based on the theory of salt formation via evaporation in shallow waters and basins. This model suggests that salt was formed in shallow water under arid conditions, represented by the “Sandbar Theory” and the “Desert Theory” [1], which correspond

to the arid environments of marine and terrestrial shallow waters, respectively. However, since the 1960s, the theory of salt formation in “deep basin–deep water” has gained momentum [2–6], and it is supported by evidence of deep-water sedimentation found in numerous large ore deposits around the world, as well as salt deposits on the seafloor and the Dead Sea [7,8]. Additionally, several salt-forming models have been proposed, including the sabkha salt-forming theory [9,10], high mountains and deep basins, oscillation and aridification, synchronous basin differentiation theory [11,12], and multi-level salt lake salt formation [13]. Recently, Sirota et al. (2018) presented a halite thickening mechanism in deep-basin hypersaline environments under arid conditions based on their analysis of the halite deposition record formed after the decline in the water level in the modern Dead Sea [6]. Previously, Roveri et al. (2014) proposed a halite forming mechanism during the Mediterranean Messinian salinity crisis, whereby supersaturated brine that formed in the peripheral basins experienced gravity flow into the sedimentary center, resulting in the deposition of rock salt [14]. These theories provide important context for understanding different rock salt mineralization models.

During the Paleogene, numerous salt-bearing basins developed in eastern China, and are characterized by thick halites and accompanying oil shale deposits. Two contrasting debates on the genesis of halite deposition in these basins have been proposed: “deep-water salt-forming” and “shallow-water salt-forming” [15]. For example, Cenozoic saline lake basins, such as the Dongpu Depression, the Dongying Depression, and the Hongze Depression in eastern China, are considered to share characteristics of “deep water evaporite deposition” [16–19]. In a stable and deep-water environment, the brine is stratified, and the salt concentration increases as the surface lake water evaporates. Under the influence of gravity, the brine migrates downward into salt deposits [11,12,16–19]. However, some scholars have identified markers of shallow-water salt-forming processes based on lithology and sedimentary structures, such as red mudstones, mud cracks, rain marks, and crossbedding [20]. Additionally, “syngenetic sandstone breccia” and “mudstone tearing debris” have been found as massive sandstones, indicating a shallow-water environment induced by the evaporation and concentration of lake water during arid climates, with a successive precipitation of carbonate, gypsum, and halite after brine saturation [21]. The newly discovered large-scale halite deposits in the Huanggang Depression in eastern China provides excellent sedimentary record and samples (i.e., continuous salt-bearing strata in the YZR1 borehole) for studying the mechanism of halite deposition, and potentially resolving the deep-water vs. shallow-water salt-forming debate in eastern China. The region is predominantly overlain by the Quaternary system, with concealed strata ranging from the Neoproterozoic Mount Taishan Group through to the Ordovician Majiagou Group, the Carboniferous–Permian Yuemengou Group, the Permian Shihezi Group, the Paleogene Guanzhuang Group, and the Neogene Huanghua Group [22].

## 2. Geological Settings

The Huanggang Depression is a fault basin that formed during the late Cretaceous period east of the North China Plate and is situated in the southwestern region of Shandong Province in eastern China at approximately 116°E longitude and 34.5°N latitude [23–26] (Figure 1). The basin is a terrestrial fault basin formed under the action of the Tantanlu strike–slip fracture system in eastern China, and a large rock salt deposit with a reserve of more than 20 billion tons was deposited during the Paleogene period. During the Eocene–Oligocene epoch, a continuous and widespread shallow and saline lacustrine succession, rich in halite, gypsum, and other salt minerals, developed in the Dawenkou Formation, Guanzhuang Group of the Huanggang Basin [22,27]. The Dawenkou Formation consists of three sections, with the lower section being primarily composed of brownish-red to purplish-red mudstone and argillaceous siltstone. The middle section contains a salt-bearing succession comprising grayish-white gypsiferous mudstone/halite interbedded with dark-gray mudstone/silty mudstone. And the upper section is predominantly composed of gray/grayish-green mudstone, yellow/light-yellow silty mudstone, and siltstone,

with occasional gravel beds at the bottom [26]. The sedimentary sequence reflects the cyclicity of the water desalination–salinization processes, with evaporation and deposition occurring from the bottom to the top of the formation (Figure 2).

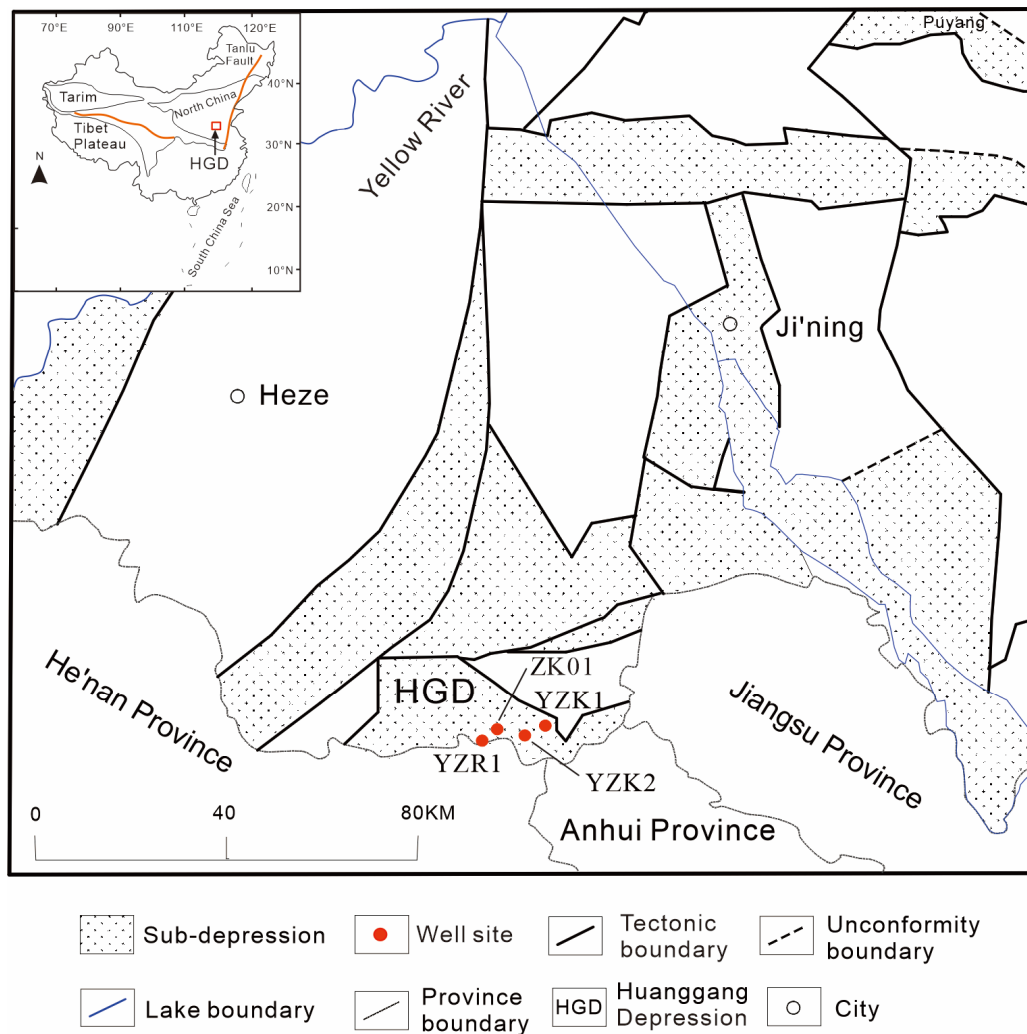


**Figure 1.** Regional tectonic map of the Huanggang Basin and adjacent localities (modified from Tang et al., 2021 [22]).

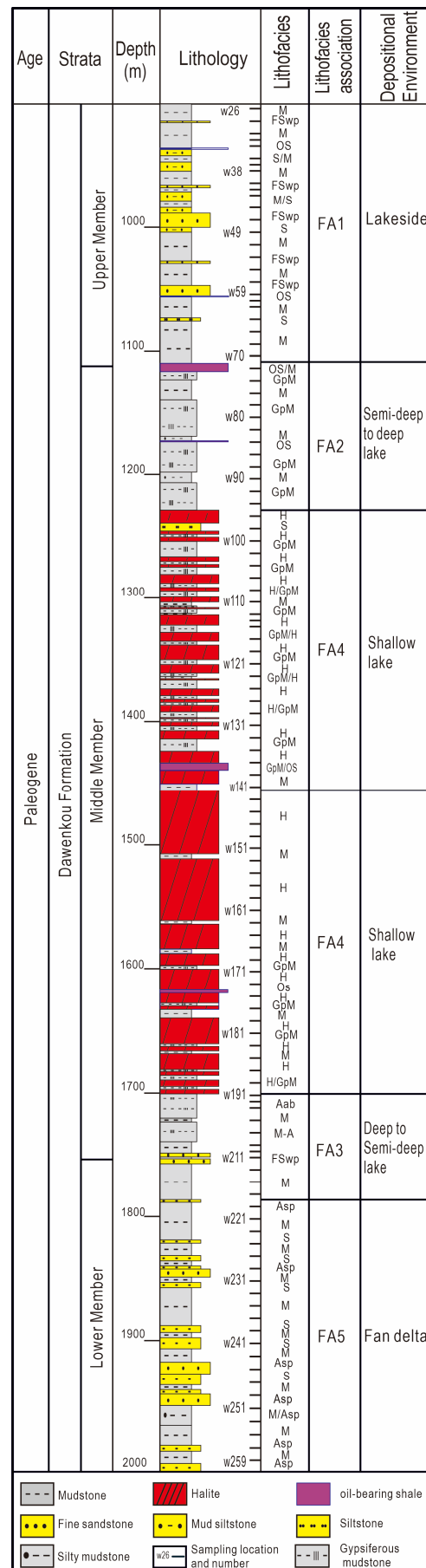
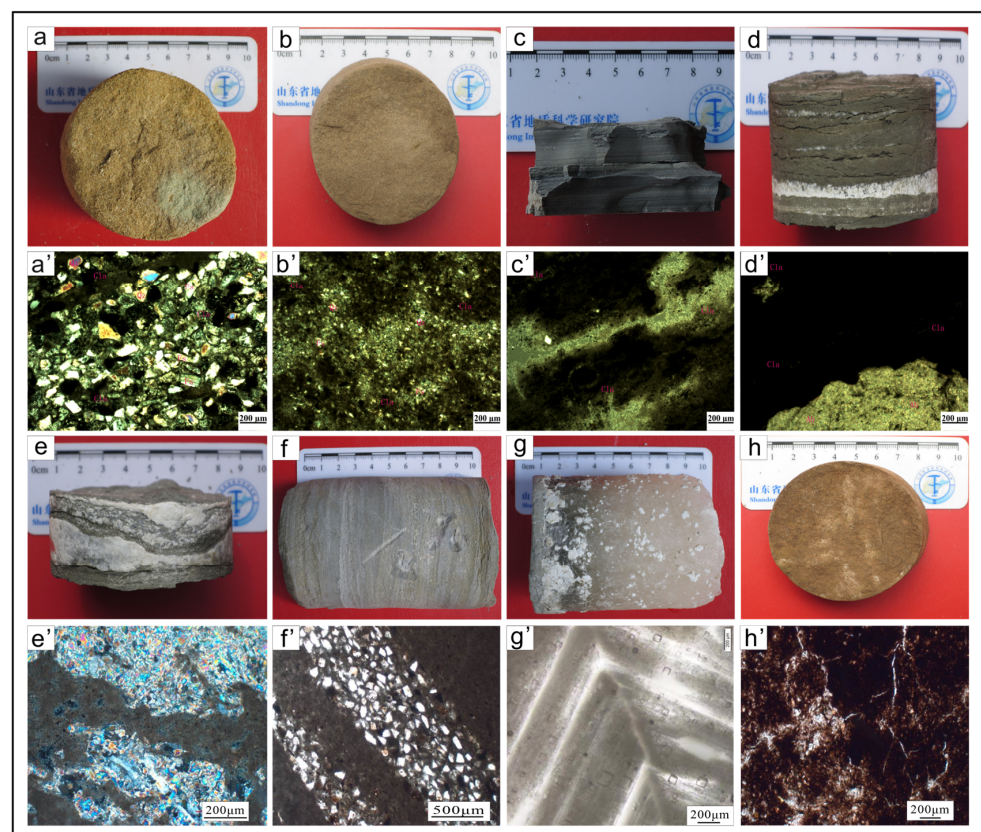


Figure 2. Stratigraphy and sedimentary facies division of YZR1 hole in the Huanggang Depression.

### 3. Sampling and Methods

We performed a sedimentological analysis by examining the petrographic characteristics of the rock core to infer the sedimentary environment. Lithofacies are commonly used to study depositional environments. In the Huanggang Depression, we sequentially drilled four boreholes (YZR1, ZK01, YZK2, and YZK1) and selected the YZR1 well, which has an entire column of lithofacies and lithofacies associations to obtain a sense of how the Dawenkou depositional environment evolved during the Paleogene. The cores from hole YZR1 were all collected continuously and are well preserved.

Mudstone and gypsiferous mudstone samples were collected every 10 m from various lithofacies of well YZR1, with densified sampling in key layers. A comprehensive set of 117 core samples was systematically retrieved from the Dawenkou Formation within the Guanzhuang Group. Specifically, 24 samples were procured from the upper section, 67 from the middle section, and the remaining 26 from the lower section of the Dawenkou Formation. Major, trace, and rare-earth element analyses were performed on all rock samples. The major elements include  $\text{Al}_2\text{O}_3$ ,  $\text{K}_2\text{O}$ ,  $\text{TiO}_2$ , and  $\text{P}_2\text{O}_5$ , and the trace elements include B, Ga, Sr, Ba, V, Ni, Mn, Cu, Th, U, etc. By conducting a meticulous examination of the lithological assemblage features in the drill cores and microscopic mineral characteristics (refer to Figures 2 and 3), coupled with advanced geochemical analysis techniques, we aimed to comprehensively characterize the sedimentary phases of the Paleoproterozoic Dawenkou Formation within the Huanggang Depression and elucidate the corresponding sedimentary phase assemblages (detailed in Tables 1 and 2).



**Figure 3.** Sedimentary characteristics of the Dawenkou Formation in the Huanggang Depression. (a–d) Light-yellow fine sandstone, purplish-red siltstone, grayish-black thin-layer mudstone, and mudstone intercalated with banded anhydrite. (a'–d') The microstructure of (a–d), respectively. (e–h) Interbedding of carbonate and anhydrite rocks, interbedding of micrite limestone and mudstone, white halite and anhydrite, and purplish-red argillaceous siltstone; (e'–h') correspond to the microstructure of (e–h).

**Table 1.** Lithofacies characteristics of well YZR1 in the Huanggang Depression.

Lithofacies Type	Feature Description	Sedimentary Environment
Wave-parrel bedding fine-grained sandstone (FSwp)	Greenish-gray to brownish-gray, containing calcareous or argillaceous cement. Clay minerals as the base material, while the clastic composition mainly consists of well-sorted medium ellipse quartz and feldspar, with a small amount of mica. Plagioclase can be seen as polycrystalline twin, and potassium feldspar can be seen as lattice twin, with pore cementation (Figure 3a).	Fluid flow under low flow conditions, deposited in braided river or delta front mouth bar [28,29].
Siltstone (S)	Purplish-red, containing thin mudstone and fine sandstone layers. The fine sandstone interlayers are generally sorted but with good roundness (Figure 3b).	Usually appears in alluvial fan depression, fan delta, or flood plain of fluvial deposit [30].
Mudstone (M)	Gray-green or gray-black, mainly composed of argillaceous minerals, silty sand, organic matter, etc. Clay minerals are microscopically scaly or cryptocrystalline, with grain size generally less than 0.004 mm. The aggregates are slightly semi-oriented, forming a weak layered structure. Silty sand is mainly composed of feldspar and quartz fragments, which are mostly angular and distributed unevenly in gaps or bedding. Biological debris of Ostracoda, Lamellibranchia, and calcium globes can be seen occasionally (Figure 3c).	Formed in a stable water environment, such as a lakeside environment or a deep to semi-deep lacustrine environment [29], or in a flood plain, such as a sedimentary crevasse fan [30], or in an alluvial fan, a depression between the braided channels of a fan-delta plain, both during the humid climate [30].
Interbedding with grey mudstone and anhydrite (M-A)	The mudstone is grayish-green or grayish-black, with a lamina thickness of 0.05~25 mm, and contains few felsic clasts, calcite, and pyrite. Illite is the dominant clay mineral distributed in scale-like direction. Angular-shaped feldspar clasts and heteromorphic granular-shaped calcite. Most anhydrite rocks are distributed in thin layers or banded layers, with thickness ranging from 0.2 to 20 mm. The anhydrite crystal is columnar, with a grain size of 0.02 to 0.8 mm (Figure 3d).	Mainly formed in the alternating environment of deep-lake evaporation and lake dilution [31].
Gypsiferous mudstone (GpM)	Mainly consists of grayish-green mudstone. Massive anhydrite is produced in mudstone, in a thin or block-mass structure. The thin-block-mass gypsum layer has an irregular and massive internal structure, such as pores, small nodules or a broken and deformed internal clastic structure. Small crystal cores in the block are often surrounded by large gypsum crystals. The massive block gypsum is formed from the hemispherical or small-nodule-shaped consolidated gypsum, without intermediate lamination (Figure 3d,e).	Thin-layer block anhydrite is commonly found in shallow lake deposits, such as shallow salt lakes. Large-block anhydrite appears in shallow-lake environment, which is shallower than that of thin-block gypsum [32].

Table 1. Cont.

Lithofacies Type	Feature Description	Sedimentary Environment
Interbedding with carbonate and anhydrite (Aab)	Composed of irregularly alternating anhydrite layers (white) and carbonate layers (dark gray). Anhydrite mainly occurs in carbonate in the form of a strip, layer, and lens, and the thickness of laminae varies from 0.2 to 20 mm. Carbonate is in an argillaceous structure, mainly composed of calcite and dolomite, in a granular shape, with grain size less than 0.01 mm, mixed with a small amount of felsic clasts (Figure 3e,f).	The alternating light and dark laminated limestone represents the dynamic environment and flood events with seasonal strong/weak alternation, which mostly occur in deep-water deposits [33,34]. The rhythm of banded and lenticular gypsum alternates and the local water ripple marks indicate that the lenticular thin gypsum layer was formed in a deep-lake environment during the lake water dilution period [31].
Halite (H)	Grayish-white or colorless, allomorphic or semi-idiomorphic grain. The grain size is about 2~10 mm. Grains are closely inlaid, with cubic cleavage developed for some particles, occasionally occurring as a 'ladder' structure. Contain terrigenous clasts, the mineral composition is mainly halite, with the thickness varying from 0.82 to 53.96 m. Primary fluid inclusions form a herringbone pattern in the chevron halite, as well as in the funnel-shaped cumulate halite (Figure 3g).	Herringbone crystal is a crystal-chemical feature of the growth of bottom halite up along the triple axis. When herringbone and funnel crystals appear at the same time, this indicates an extremely shallow water environment [35–37].
Oil shale (OS)	Yellowish-brown, locally mixed with siltstone and mudstone, containing horizontal bedding, argillaceous texture, and foliation texture, with thickness almost always greater than 1 m, containing bioclastic.	Formed in the still-water environment of a semi-salty to salty shallow lake under a humid and hot climate. The highest dry-hot degree during the dry/wet alternation process at this stage has not reached the halite precipitation state [38].
Purplish-red Argillaceous Siltstone (ASp)	Light red or purplish-red, porous cementation, consisting of quartz, feldspar, clay minerals, carbonate, and muddy particles. Angular-shaped detritus, with a grain size of 0.02~0.25 mm, mainly feldspathic clasts, little mica. The clay mineral of the base materials is mainly illite, microscopically scaly. The carbonate is mainly calcite, which is in an allomorphic granular shape, and the particle size is less than 0.05 mm (Figure 3h).	Usually appears in alluvial fan, fan delta, or fluvial deposits [31]. Generally, it is the product of turbidite sandy sediment mixed with deep-lake muddy sediment, which may be the result of periodic turbidite events [29].

Table 2. Typical lithofacies assemblage characteristics of well YZR1 in the Huanggang Depression.

Number	Assemblages	Sedimentary Environment and Characteristics
FA1	FSwp, M, S	Lakeside environment, with laminae at the bottom
FA2	M, GpM	Deep to semi-deep lacustrine environment, commonly developed laminae
FA3	M-A, Aab	Semi-deep to deep saline lacustrine environment, with laminae
FA4	H, GpM, OS	Shallow saline lacustrine environment
FA5	ASp, M, S	Fan delta (turbidity current deposits) without laminae

The major and trace element analyses of the rock samples were conducted at the Shandong Academy of Geological Sciences (Jinan Mineral Resources Supervision and Inspection Center of the Ministry of Natural Resources of Shandong Province, Jinan, China), a research institution in the field of Earth sciences. We utilized a constant chemical analysis and inductively coupled plasma atomic emission spectrometry (ICP-AES, Thermo

Fisher iCAP-7400, Waltham, MA, USA) for the primary and secondary elemental analysis, as well as inductively coupled plasma mass spectrometry (ICP-MS, Thermo Fisher iCAP RQ, Waltham, MA, USA) for the trace and rare-earth element analyses. Measurement errors were generally less than 5%. The paleoclimatic and paleoenvironmental conditions during sedimentation were assessed using the multi-element ratio of sensitive elements. (1) The B/Ga and Sr/Ba ratios are used to assess the paleosalinity during the sedimentation process; the criteria for the delineation of paleosalinity were adopted from previous studies. (2) The (V + Ni + Mn) ratio and major element ratios of Al<sub>2</sub>O<sub>3</sub>, K<sub>2</sub>O, TiO<sub>2</sub>, and P<sub>2</sub>O<sub>5</sub> are used to assess the paleowater depth. (3) The Sr/Cu ratio is used to assess the paleoclimate. (4) The V/(V + Ni) ratio and  $\delta U$  are used to assess the oxidation reduction state of the sedimentary environment, which can be calculated using the formula  $\delta U = U/[0.5 \times (U + Th/3)]$ .

## 4. Results

### 4.1. Lithofacies and Lithofacies Associations

We identified nine lithofacies and five lithofacies assemblages from our analysis of the petrological and sedimentary structural characteristics of rock cores obtained from the Huanggang Depression (Table 1). Each assemblage provides insights into the corresponding sedimentary environment (Table 2 and Figure 3).

The lithofacies assemblage FA1 comprises three facies: wave-parallel-bedding fine-grained sandstone (FSwp), mudstone (M), and siltstone (S). FSwp is primarily composed of quartz and feldspar, with a small amount of dark minerals, and exhibits moderate rounding and good sorting of its debris [29]. The mudstone in this environment is a bioclastic due to sufficient oxygen and sunlight. The expansion of the lake during the lakeshore facies deposition process resulted in the regional formation of oil shale. Unstable oil shale deposits suggest limited deep-water areas for algae deposition [39–42].

The lithofacies assemblage FA2 consists of mudstone (M) and gypsiferous mudstone (GpM) facies, which are indicative of deep to semi-deep lacustrine facies. The absence of wave action in the deep-water environment and anoxic conditions resulted in the formation of fine-grained sedimentary rock with a darker hue. Laminated and alternating laminated structures commonly develop in evaporite. The upper dark-gray to gray–black mudstone and bottom laminated gypsum are horizontally layered, suggesting a deep to semi-deep lake sedimentary environment [29]. The development of wavy bedding at intermediate depths indicates the influence of rivers or seasonal floods.

The lithofacies assemblage FA3 comprises grey mudstone (M-A) and carbonate (Aab) facies, both interbedded with anhydrite. The FA3 facies assemblage represents a transitional phase from a salt to a freshwater lake. Blocky anhydrites commonly develop near thin intervals of halite layers, indicating a concurrent evaporation during deposition. Secondary nodular gypsum and banded secondary gypsum are visible at locations further away from the halite layers. We infer that the primary evaporite may have been transformed into secondary rock due to atmospheric precipitation, groundwater, or flood season. This lithofacies assemblage is interpreted as deep to semi-deep saline lake facies.

The lithofacies assemblage FA4 comprises three lithofacies: grayish-white halite (H), gypsiferous mudstone (GpM), and oil shale (OS). The FA4 facies has a thickness of approximately 260 m. This assemblage indicates a shallow salt lake sedimentary environment located below the wave base surface. It is characterized by a weak redox environment with moderate to weak hydrodynamic forces and a high organic matter content. Interbeddings of evaporates, such as halite, lenticular/agglomerate anhydrite, dolomitic mudstone, and oil shale, occur under dry conditions. There is a limited sedimentary record of biologic activity due to the high salinity. The alternating combination of halite, anhydrite, and mudstone in the longitudinal direction indicates the frequent expansion and contraction of the lake.

The lithofacies assemblage FA5 comprises purplish-red argillaceous siltstone (ASp), mudstone (M), and siltstone (S). The purplish-red siltstone and argillaceous siltstone are typically a mixture of sandy turbidite and deep-lake muddy sediments, possibly due to

periodic turbidite events [30]. The purplish-red and grayish-green alternating colors of silty mudstone gradually transition upward in successions of weak laminae. A small amount of laminated anhydrite is intercalated at the top. This lithofacies assemblage indicates a deeper water environment, likely a fan-delta turbidite sedimentary environment supplemented by surface runoff.

#### 4.2. Elemental Geochemistry

Trace elements are usually preserved, and they reflect the original geochemical composition of the paleoenvironmental conditions at the time of deposition. This study provides a detailed statistical analysis of 117 main and trace element test results from the YZR1 well in the Huanggang Depression, and we conducted a phased comparative analysis based on the change characteristics.

In the lower section (2005.99–1753.53 m) of the Dawenkou Formation, the average B/Ga value of 24 samples is 2.74, with a maximum value of 4.91. Among these samples, 15 fall within the range of 1.28 to 3. The average Sr/Ba ratio is 0.65, with 12 samples distributed between 0.35 and 0.5. The Th/U ratio within the 23 samples exhibits a distribution ranging from 1.74 to 3.52, with an average value of 4.28 and a single sample registering a value of 0.11. All samples in this section have combined values of V + Ni + Mn exceeding 190 µg/g, with an average value of 760.57 µg/g. The Sr/Cu ratios range from 2.38 to 89.53, with an average value of 26.92. Among these values, 19 samples exceed 10, while five samples fall below this threshold. The V/(V + Ni) ratios of 23 samples fall between 0.60 and 0.84, with an average value of 0.72. Only one sample exhibits a ratio lower than 0.60 (Figure 4 and Table 3).

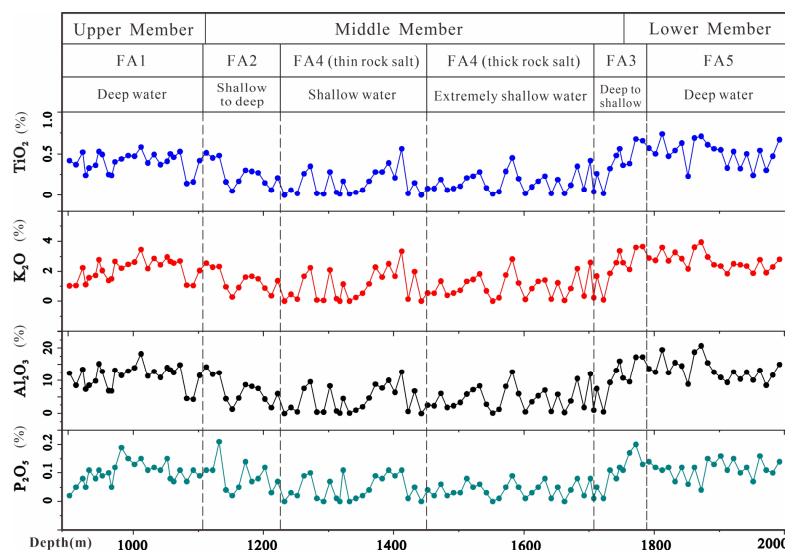


Figure 4. Variation diagram of the trace element contents and ratios in core YZR1 of the Huanggang Depression.

Table 3. The elemental geochemical analysis data of well YZR1 in Huanggang Depression.

Depth (m)	Sample No.	Lithology	Trace Element Content								Main Element Content					
			B (µg/g)	Ga (µg/g)	Sr (µg/g)	Ba (µg/g)	V (µg/g)	Ni (µg/g)	Cu (µg/g)	U (µg/g)	Th (µg/g)	MnO (%)	Al <sub>2</sub> O <sub>3</sub> (%)	K <sub>2</sub> O (%)	TiO <sub>2</sub> (%)	P <sub>2</sub> O <sub>5</sub> (%)
902	w26	Mudstone	31.98	13.55	201.20	795.60	44.74	17.81	16.68	0.82	7.08	0.0487	12.31	1.02	0.42	0.02
912	w28	Mudstone	28.03	11.62	176.00	965.30	67.32	40.17	17.57	1.53	7.66	0.4094	8.54	1.06	0.37	0.05
922	w30	Mudstone	55.26	18.69	600.60	1205.0	72.86	40.52	21.81	3.96	12.89	0.0777	13.40	2.22	0.52	0.08
927	w32	Mudstone	23.42	10.25	175.20	701.80	33.39	11.09	9.80	1.98	6.63	0.1430	7.40	1.12	0.24	0.05
932	w33	Mudstone	39.71	11.05	502.30	644.90	38.82	13.55	10.61	2.23	8.24	0.1183	8.57	1.57	0.33	0.11
942	w35	Mudstone	46.22	12.89	598.10	427.30	47.81	16.70	12.95	3.26	9.11	0.0869	9.82	1.72	0.36	0.08
947	w37	Mudstone	83.16	20.98	404.70	365.60	73.61	20.96	15.75	2.28	13.14	0.0602	15.09	2.77	0.53	0.11

Table 3. Cont.

Depth (m)	Sample No.	Lithology	Trace Element Content								Main Element Content					
			B (µg/g)	Ga (µg/g)	Sr (µg/g)	Ba (µg/g)	V (µg/g)	Ni (µg/g)	Cu (µg/g)	U (µg/g)	Th (µg/g)	MnO (%)	Al <sub>2</sub> O <sub>3</sub> (%)	K <sub>2</sub> O (%)	TiO <sub>2</sub> (%)	P <sub>2</sub> O <sub>5</sub> (%)
952	w38	Mudstone	72.24	17.59	653.50	256.10	66.70	25.76	20.19	4.16	12.30	0.0763	12.83	2.04	0.49	0.09
962	w40	Mudstone	39.10	9.94	698.50	430.20	37.09	16.22	11.14	2.24	6.68	0.0669	6.88	1.38	0.25	0.10
967	w41	Mudstone	35.08	9.27	794.30	355.20	32.46	14.35	9.52	1.57	5.99	0.0549	6.83	1.50	0.24	0.05
972	w43	Mudstone	54.80	18.12	533.70	216.20	62.27	19.76	17.80	2.26	11.08	0.0516	13.25	2.65	0.40	0.12
982	w45	Mudstone	69.18	15.94	561.50	444.80	59.25	21.52	17.14	3.21	11.33	0.0965	11.62	2.20	0.44	0.19
992	w47	Mudstone	62.33	17.20	512.40	574.50	61.77	22.59	13.58	2.42	12.10	0.0613	12.94	2.46	0.48	0.15
1002	w49	Mudstone	87.18	19.03	5158.0	987.30	69.21	22.03	19.62	3.71	13.02	0.0688	13.88	2.61	0.47	0.13
1012	w51	Mudstone	65.84	24.78	851.00	403.60	90.01	25.46	19.42	2.79	14.64	0.0494	18.15	3.45	0.58	0.15
1022	w53	Mudstone	73.03	15.46	1072.0	384.20	59.08	18.92	15.66	3.13	10.68	0.0646	11.39	2.18	0.39	0.11
1032	w55	Mudstone	78.35	17.33	671.00	460.10	66.41	23.90	19.58	3.59	12.12	0.0694	12.84	2.86	0.49	0.12
1042	w57	Mudstone	68.35	15.05	778.40	326.30	52.17	16.68	14.24	2.28	9.75	0.0464	10.98	2.43	0.37	0.11
1052	w59	Carbonate	89.73	19.23	604.00	235.40	62.97	21.12	17.20	2.56	11.85	0.0419	14.05	2.94	0.41	0.15
1057	w61	Mudstone	77.36	18.83	539.50	441.80	67.86	23.67	20.93	3.73	13.22	0.0659	13.29	2.66	0.50	0.08
1062	w62	Mudstone	54.55	18.37	1127.0	384.10	72.81	27.23	23.79	4.01	13.29	0.0775	12.54	2.54	0.46	0.07
1072	w64	Mudstone	95.78	20.28	318.30	346.80	74.49	23.58	24.13	2.99	13.78	0.0481	14.78	2.68	0.53	0.11
1082	w66	Mudstone	29.74	6.58	807.00	177.00	22.37	9.48	6.77	0.94	3.83	0.0459	4.58	1.08	0.14	0.07
1092	w68	Carbonate	28.32	6.18	869.30	204.10	23.92	11.05	6.45	1.40	4.11	0.0406	4.23	1.06	0.16	0.11
1102	w70	Mudstone	64.40	15.95	1020.0	181.70	61.56	24.46	19.32	3.57	10.99	0.0675	11.59	2.04	0.42	0.09
1112	w72	Oil shale	70.23	21.30	679.80	278.50	82.04	33.78	30.87	4.60	13.29	0.0851	14.20	2.54	0.51	0.11
1122	w74	Mudstone	65.27	15.39	1373.0	504.90	56.35	20.97	16.70	3.90	12.31	0.0692	12.03	2.27	0.45	0.11
1132	w76	Mudstone	89.52	16.62	1863.0	560.40	71.20	25.37	20.81	3.70	11.96	0.0749	12.37	2.32	0.48	0.21
1142	w78	Gypsiferous mudstone	37.38	6.15	3950.0	366.60	23.57	9.41	7.50	1.26	4.35	0.0191	4.47	0.95	0.16	0.04
1152	w80	Gypsiferous mudstone	11.64	1.98	1922.0	59.25	6.89	5.12	3.71	0.39	1.27	0.0068	1.26	0.29	0.05	0.02
1162	w82	Gypsiferous mudstone	39.17	6.52	2073.0	164.40	25.30	10.21	7.83	1.57	4.76	0.0296	4.68	0.92	0.17	0.05
1172	w84	Oil shale	35.97	12.42	1093.0	268.90	49.30	21.73	18.31	4.19	8.71	0.0688	8.72	1.61	0.30	0.14
1182	w86	Gypsiferous mudstone	79.87	10.64	2410.0	433.80	38.30	13.74	11.51	2.69	8.01	0.0413	8.20	1.66	0.29	0.07
1192	w88	Gypsiferous mudstone	86.83	10.38	2478.0	409.00	39.57	14.30	10.97	2.31	7.62	0.0569	7.66	1.50	0.27	0.08
1202	w90	Gypsiferous mudstone	45.71	6.29	2139.0	520.90	26.40	9.58	6.79	1.41	4.17	0.0499	4.39	0.86	0.15	0.12
1212	w92	Gypsiferous mudstone	17.17	2.60	2865.0	132.20	9.33	5.40	3.98	0.72	1.65	0.0190	1.73	0.37	0.06	0.03
1222	w94	Gypsiferous mudstone	77.23	8.14	2883.0	254.40	30.02	12.19	9.78	2.06	5.94	0.0282	5.97	1.37	0.21	0.07
1232	w96	Halite	1.20	0.46	199.00	5.88	<0.3	0.61	0.41	0.06	0.06	0.0011	0.03	0.01	0.00	0.00
1242	w98	Halite	17.56	2.58	4325.0	130.00	9.93	6.17	4.58	0.70	1.69	0.0091	1.86	0.46	0.06	0.03
1252	w100	Halite	3.96	1.05	543.70	19.69	3.62	2.37	1.64	0.19	0.49	0.0100	0.50	0.14	0.02	0.02
1262	w102	Gypsiferous mudstone	79.96	10.29	243.80	191.30	39.10	15.21	12.50	2.56	7.31	0.0574	7.58	1.65	0.26	0.09
1272	w104	Mudstone	80.04	12.23	1418.0	537.40	45.62	16.28	13.06	2.57	8.63	0.0526	9.64	2.22	0.35	0.10
1282	w106	Halite	2.84	0.79	692.40	20.28	2.23	1.67	1.29	0.14	0.36	0.0023	0.37	0.08	0.02	0.01
1292	w108	Halite	3.28	0.78	36.76	10.08	2.24	1.33	1.20	0.15	0.28	0.0027	0.34	0.06	0.01	0.00
1302	w110	Mudstone	75.99	10.33	1573.0	388.30	33.95	12.74	9.99	2.00	6.91	0.0367	8.35	2.08	0.28	0.07
1312	w112	Halite	3.71	1.25	1349.0	43.67	3.47	3.15	2.41	0.28	0.68	0.0036	0.71	0.18	0.03	0.01
1317	w113	Halite	1.69	0.43	179.10	7.03	<0.3	0.83	0.63	0.14	0.07	0.0012	0.06	0.02	0.01	0.00
1322	w115	Mudstone	54.18	6.15	623.30	248.60	23.31	9.98	6.90	1.33	4.29	0.0588	4.55	1.13	0.17	0.11
1332	w117	Halite	1.41	0.37	1281.0	13.10	<0.3	0.95	0.58	0.11	0.06	0.0012	0.04	0.01	0.01	0.00
1342	w119	Gypsiferous mudstone	8.65	1.64	2468.0	53.71	5.02	3.34	2.29	0.32	0.82	0.0069	1.00	0.26	0.03	0.01
1352	w121	Halite and anhydrite	10.38	2.74	1517.0	104.90	8.04	4.13	3.31	0.59	1.51	0.0076	1.97	0.54	0.06	0.02
1362	w123	Gypsiferous mudstone	40.57	6.04	4418.0	244.90	20.78	9.89	8.12	1.51	4.08	0.0187	4.69	1.16	0.17	0.04
1372	w125	Halite and anhydrite	124.64	11.86	3251.0	288.80	44.72	15.80	13.92	2.29	7.84	0.0469	8.86	2.26	0.28	0.09
1382	w127	Mudstone	122.08	10.07	1796.0	358.40	42.87	16.12	16.22	2.96	7.55	0.0531	7.73	1.61	0.28	0.08
1392	w129	Mudstone	127.78	13.32	568.00	252.30	49.12	25.90	23.41	3.11	9.92	0.0521	10.02	2.50	0.39	0.11
1402	w131	Gypsiferous mudstone	48.35	7.74	765.30	391.10	22.98	9.13	6.93	1.33	4.76	0.0600	6.34	1.66	0.21	0.09
1412	w133	Gypsiferous mudstone	211.90	16.01	262.50	387.70	55.98	24.51	20.66	2.67	12.39	0.0446	12.68	3.33	0.56	0.11
1422	w135	Halite	6.78	1.11	703.20	31.43	2.86	1.77	1.33	0.24	0.59	0.0044	0.58	0.14	0.02	0.01
1432	w137	Oil shale	23.16	7.68	280.20	504.90	14.22	7.01	4.71	1.35	4.25	0.0263	6.81	1.98	0.15	0.05
1442	w139	Halite	1.02	0.45	1193.0	16.02	0.74	0.75	0.83	0.11	0.07	0.0025	0.02	0.01	0.00	0.00
1452	w141	Mudstone	34.03	3.85	2677.0	141.70	13.18	7.29	5.48	0.81	2.48	0.0217	2.56	0.56	0.08	0.04
1462	w143	Mudstone	44.51	3.40	3270.0	180.80	11.16	6.30	4.87	0.96	2.25	0.0211	2.33	0.54	0.08	0.02
1472	w145	Mudstone	124.20	8.46	1633.0	235.50	26.94	9.92	9.34	1.59	5.34	0.0305	6.10	1.34	0.19	0.06
1482	w147	Carbonate	25.58	2.54	2294.0	111.40	8.45	4.96	3.79	0.68	1.60	0.0195	1.81	0.39	0.06	0.02
1492	w149	Carbonate	18.83	3.38	1861.0	133.30	10.90	5.93	4.14	0.84	2.04	0.0140	2.35	0.56	0.08	0.03
1502	w151	Halite	46.06	4.66	2042.0	138.90	14.69	7.14	5.44	1.01	3.03	0.0241	3.33	0.74	0.11	0.03
1512	w153	Mudstone	86.85	8.16	1228.0	173.20	32.10	13.16	10.57	1.88	5.60	0.0486	5.85	1.33	0.21	0.08
1522	w155	Mudstone	106.24	9.79	2754.0	213.40	33.51	13.69	11.70	2.29	6.47	0.0284	7.16	1.46	0.23	0.05
1532	w157	Gypsiferous mudstone	154.19	11.26	2527.0	330.50	43.18	16.48	13.89	3.32	7.69	0.0379	8.33	1.81	0.28	0.06
1542	w159	Mudstone	33.34	3.94	1886.0	141.40	13.13	6.62	5.72	1.01	2.51	0.0188	2.74	0.68	0.09	0.03
1552	w161	Halite	1.28	0.46	121.80	8.13	<0.3	0.77	0.63	0.07	0.10	0.0009	0.05	0.02	0.01	0.00

Table 3. Cont.

Depth (m)	Sample No.	Lithology	Trace Element Content								Main Element Content					
			B (µg/g)	Ga (µg/g)	Sr (µg/g)	Ba (µg/g)	V (µg/g)	Ni (µg/g)	Cu (µg/g)	U (µg/g)	Th (µg/g)	MnO (%)	Al <sub>2</sub> O <sub>3</sub> (%)	K <sub>2</sub> O (%)	TiO <sub>2</sub> (%)	P <sub>2</sub> O <sub>5</sub> (%)
1562	w163	Mudstone	9.20	1.92	1937.0	29.18	5.49	4.60	3.22	0.35	1.08	0.0059	1.17	0.24	0.04	0.01
1572	w165	Halite and anhydrite	91.94	11.08	1635.0	290.70	38.93	15.04	12.14	2.02	7.34	0.0278	8.24	1.75	0.29	0.05
1582	w167	Oil shale	130.77	16.55	1037.0	484.80	58.63	22.21	20.02	3.71	11.50	0.0525	12.65	2.81	0.45	0.09
1592	w169	Gypsiferous mudstone	116.96	8.16	2387.0	279.30	30.07	12.13	10.40	1.94	5.45	0.0308	5.96	1.22	0.20	0.05
1602	w171	Halite	4.87	1.01	2130.0	40.57	2.52	2.68	1.84	0.22	0.45	0.0032	0.50	0.12	0.02	0.01
1612	w173	Oil shale	31.33	4.45	1190.0	214.40	12.04	5.62	4.88	0.96	2.35	0.0159	3.52	0.84	0.10	0.03
1622	w175	Oil shale	66.76	6.90	1197.0	303.80	19.50	8.36	7.03	1.38	4.71	0.0291	5.36	1.32	0.17	0.05
1632	w177	Gypsiferous mudstone	93.52	9.64	2203.0	315.20	38.15	14.88	12.39	4.27	6.80	0.0566	7.13	1.41	0.23	0.08
1642	w179	Gypsiferous mudstone	3.03	1.17	967.80	29.09	3.13	2.55	1.76	0.23	0.59	0.0063	0.64	0.14	0.02	0.01
1652	w181	Halite	58.49	7.48	1343.0	252.10	23.78	9.71	8.44	1.76	5.07	0.0316	5.81	1.23	0.19	0.05
1662	w183	Halite	3.05	0.92	182.30	19.49	1.70	1.27	1.21	0.18	0.32	0.0045	0.32	0.06	0.02	0.00
1672	w185	Gypsiferous mudstone	37.38	5.22	2927.0	257.60	15.73	7.00	6.24	1.34	3.20	0.0224	3.74	0.85	0.12	0.04
1682	w187	Gypsiferous mudstone	174.16	13.83	767.30	293.80	51.83	18.22	16.47	3.17	9.42	0.0692	10.53	2.19	0.35	0.08
1692	w189	Halite	13.92	2.85	261.70	69.48	7.38	3.32	3.25	0.45	1.62	0.0116	1.82	0.36	0.07	0.02
1702	w191	Mudstone	158.36	16.49	1318.0	458.80	58.40	21.46	20.12	3.50	10.58	0.0540	12.10	2.58	0.42	0.08
1707	w193	Mudstone	10.96	1.70	3162.0	93.51	5.34	5.32	3.39	0.43	1.03	0.0051	1.01	0.24	0.04	0.01
1712	w194	Mudstone	84.59	10.19	3066.0	309.70	34.56	14.51	12.01	2.58	7.05	0.0345	7.55	1.69	0.26	0.05
1722	w196	Mudstone	5.12	0.99	1962.0	16.87	2.49	4.14	2.54	0.17	0.53	0.0023	0.48	0.10	0.02	0.01
1732	w198	Mudstone	78.89	12.56	516.90	156.60	44.62	15.80	13.62	3.07	8.57	0.0640	9.49	1.87	0.32	0.11
1742	w200	Mudstone	82.99	17.64	770.60	299.20	65.12	26.31	21.05	4.29	13.31	0.0721	13.12	2.56	0.48	0.08
1747	w201	Mudstone	115.56	21.52	2884.0	526.80	84.59	28.90	27.33	4.15	14.06	0.0715	15.95	3.35	0.56	0.12
1752	w211	Argillaceous siltstone	25.56	11.07	385.30	737.80	31.04	8.42	7.58	1.44	6.98	0.0559	10.76	2.56	0.36	0.11
1762	w213	Mudstone	38.29	11.89	990.40	526.80	44.64	26.70	14.58	3.94	8.55	0.0988	9.63	2.12	0.38	0.17
1772	w215	Mudstone	80.88	23.41	198.90	494.60	99.37	30.59	21.61	3.84	15.55	0.1082	17.21	3.58	0.68	0.20
1782	w217	Mudstone	79.58	22.92	299.40	561.20	103.93	33.51	21.14	3.17	15.58	0.0982	17.28	3.65	0.66	0.13
1792	w219	Mudstone	59.99	18.68	439.20	395.40	66.41	25.36	19.03	3.30	13.63	0.0825	13.68	2.88	0.57	0.14
1802	w221	Mudstone	40.71	15.79	275.30	663.80	59.30	19.42	12.83	2.35	10.89	0.1120	12.56	2.72	0.50	0.12
1812	w223	Mudstone	77.04	26.15	192.40	532.70	109.70	33.24	24.79	3.72	17.36	0.0672	19.41	3.59	0.74	0.11
1822	w225	Mudstone	37.88	15.53	302.50	639.70	60.25	18.24	15.94	2.06	9.86	0.0858	12.43	2.71	0.47	0.12
1832	w227	Mudstone	65.16	19.36	276.30	509.90	78.08	28.91	23.53	2.84	12.43	0.0334	15.50	3.26	0.54	0.07
1842	w229	Argillaceous siltstone	65.83	19.26	276.30	691.40	77.54	25.98	15.95	3.11	14.30	0.0898	14.49	2.84	0.63	0.12
1852	w231	Carbonate	1.19	0.64	1249.0	143.30	<0.3	6.53	1.39	2.15	0.23	0.1530	8.97	2.15	0.23	0.06
1862	w233	Argillaceous siltstone	74.61	25.81	175.10	503.20	99.76	31.13	24.64	4.05	17.80	0.0569	18.65	3.60	0.69	0.12
1872	w235	Mudstone	74.96	27.93	124.60	315.60	127.97	34.30	52.55	3.37	16.83	0.0221	20.64	3.94	0.71	0.04
1882	w237	Mudstone	59.80	21.24	393.50	417.30	87.59	32.19	21.35	3.73	15.23	0.0976	15.47	2.96	0.61	0.15
1892	w239	Mudstone	46.56	17.24	266.00	706.00	68.06	23.77	21.87	2.82	11.97	0.1009	12.61	2.42	0.56	0.13
1902	w241	Argillaceous siltstone	46.27	12.71	392.60	749.20	48.08	13.38	10.31	2.64	12.83	0.1110	11.00	2.33	0.55	0.16
1912	w243	Mudstone	19.61	12.55	1325.0	710.20	54.59	17.18	14.84	4.99	8.69	0.1045	9.46	1.84	0.33	0.11
1922	w245	Argillaceous siltstone	39.61	15.96	358.60	682.00	60.03	18.88	12.42	2.59	13.30	0.0886	12.65	2.50	0.53	0.15
1932	w247	Sandstone	18.88	11.16	312.10	800.60	31.17	9.35	8.66	1.45	7.08	0.0870	10.44	2.43	0.32	0.10
1942	w249	Argillaceous siltstone	34.71	16.57	272.50	697.10	57.48	19.72	13.14	3.48	11.52	0.0803	12.58	2.34	0.50	0.12
1952	w251	Sandstone	13.34	10.39	464.70	677.30	24.78	8.13	5.81	1.21	5.74	0.0504	10.11	1.87	0.24	0.07
1962	w253	Mudstone	36.62	17.50	413.90	817.20	70.85	22.82	31.50	2.60	12.53	0.0778	13.09	2.76	0.54	0.16
1972	w255	Mudstone	52.62	10.71	734.10	321.70	41.55	14.68	11.76	2.46	7.63	0.0542	8.52	1.90	0.30	0.11
1982	w257	Mudstone	45.28	14.99	304.70	350.00	55.85	17.62	12.64	2.51	11.18	0.1300	11.69	2.29	0.47	0.10
1992	w259	Mudstone	39.95	20.70	207.30	576.40	84.01	30.18	22.40	2.65	14.07	0.0873	14.94	2.79	0.67	0.14

Moving to the middle section (1753.53–1112.17 m), the B/Ga values of 67 samples exhibit a distribution between 2.29 and 14.69, with an average value of 7.05. Out of these, 41 samples exceed six. The Sr/Ba ratios in this section range from 0.52 to 74.47, with an average of 14.79. Among the tested samples, 64 exceed a ratio of one. The Th/U ratios of all samples are distributed within the range of 0.52 to 4.86, with an average value of 2.74, and the majority of ratios fall between two and four. The combined values of V + Ni + Mn range from 8.05 to 677.08, with an average value of 267.99 µg/g. Among these values, 30 samples fall below 190 µg/g. The Sr/Cu ratios consistently exceed 10, with an average of 350.17. The V/(V + Ni) ratios range from 0.24 to 0.79, with an average of 0.64. Sixteen samples exhibit ratios lower than 0.60 (Figure 4 and Table 3).

Lastly, in the upper section (1112.17–900 m), the average B/Ga value of 26 samples is 3.77, with all samples falling within the range of two to six. The average Sr/Ba ratio is 2.08,

and 13 samples exhibit ratios below two. Additionally, out of the 12 samples in the lower portion of this section, nine exceed a ratio of 2.11. The Th/U values of all samples range from 2.79 to 5.77, with an average of 3.85. The values of V + Ni + Mn for the 26 samples in the upper section exceed 190 µg/g, with an average value of 604.41 µg/g. These samples are distributed between 10 and 263.16, with an average value of 53.09. This suggests a relatively low ratio in the upper portion. Furthermore, the Sr/Cu ratios for all samples fall within the range of 10 to 263.16, with an average of 53.09, and the majority of ratios are concentrated between 20 and 90. The V/(V + Ni) ratios in the upper section consistently fall between 0.63 and 0.78, with an average value of 0.73 (Figure 4 and Table 3).

The variations in Al<sub>2</sub>O<sub>3</sub>, K<sub>2</sub>O, TiO<sub>2</sub>, P<sub>2</sub>O<sub>5</sub>, and other major elements show a consistent pattern. The middle section of the Dawenkou Formation exhibits relatively low concentrations, while the lower and upper sections have higher concentrations (Figure 5 and Table 3).

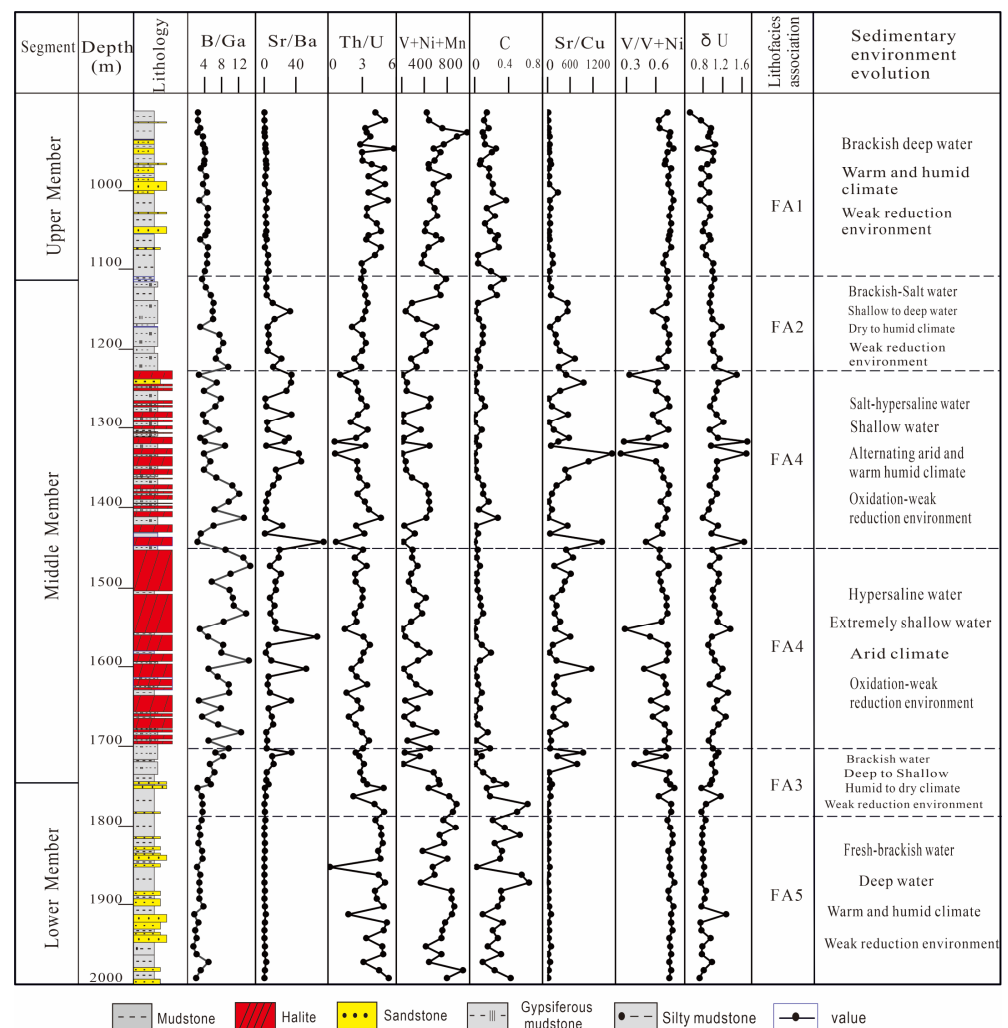


Figure 5. Variation diagram of the major element contents and ratios in core YZR1 of the Huanggang Depression.

### 5. Discussion

#### 5.1. Sedimentary Environment Evolution

##### 5.1.1. Sedimentary Environment Inferred from Lithofacies

In the lower section of the Dawenkou Formation, specifically in the middle and lower part of FA5, there is predominant deposition of purple-red and brick-red fine sandstone and siltstone. As the sandstone layers gradually decrease upwards, the proportion of siltstone increases. These sediments continuously deposit in four boreholes, namely YZR1,

ZK01, YZK2, and YZK1. The initial depth of the deposition, centered around borehole ZK01, gradually becomes shallower towards both sides, indicating a probable deposition in a fan-delta environment. The sandstone layers gradually decrease while the shale layers increase up-section, indicating a fan-delta depositional environment. No deposits of halite or gypsum are observed during this period, and there is a lack of laminations, suggesting turbid-flow deposition under warm and humid climatic conditions (Figures 2 and 6). The lake basin at the period of deposition appears to be in a compensational state with relatively high water levels.

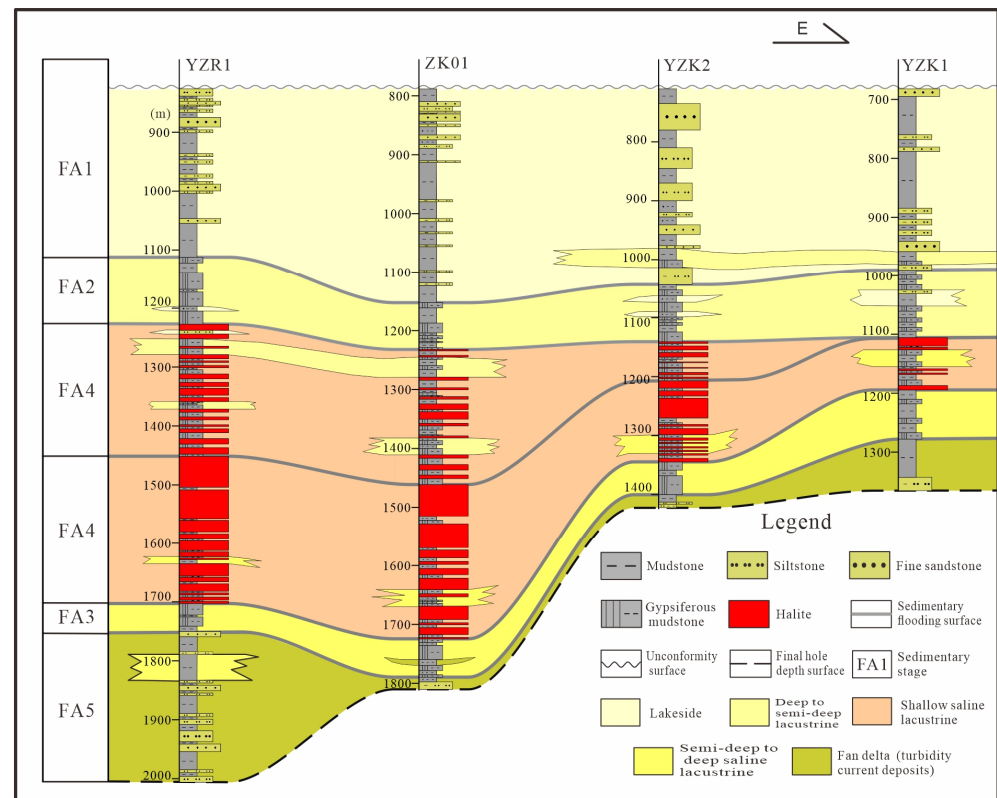


**Figure 6.** Sedimentary facies and sedimentary stage division comparison of Dawenkou Formation in Huanggang Depression.

The upper part of the lower section of the Dawenkou Formation (FA3) is mainly composed of shale deposits with a small amount of siltstone due to a dynamic equilibrium between the sediment transport mechanism and sedimentation. Towards the lower part of the middle section of the Dawenkou Formation (FA3), there is the appearance of gypsum-bearing shale, with gypsum mainly occurring as thin layer-like lenses. A small amount of thin-bedded rock salt deposits are present, indicating a transition from a warm and humid climate to a more arid one. This increase in salinity suggests a deep-lake to semi-deep-lake depositional environment.

The middle and lower part of the middle section of the Dawenkou Formation (FA4) is characterized by thick rock salt deposits with interspersed gypsum-bearing shale, indicating that arid conditions persisted. Gypsum mainly occurs as nodules and massive gypsum, with an increasing thickness of continuous rock salt deposits and massive salt beds. There is a presence of cruciform shapes and a few funnel crystals in these salt beds, likely from fluid inclusions. When herringbone and funnel crystals appear at the same time, this indicates extremely shallow water with high salinity associated with a shallow-lake depositional environment [35–37].

As the arid conditions weaken and transition to a semi-arid climate, thin-bedded rock salt with interbedded gypsum-bearing shale and shale were intermittently deposited in the

middle and upper part of the middle Dawenkou Formation (FA4). This suggests periodic climatic changes, with shallow water and relatively high salinity, indicating continued shallow-lake depositional conditions.

The upper part of the middle section of the Dawenkou Formation (FA2) primarily consists of gypsum-bearing shale and shale reflecting a transition from arid/semi-arid to warm and humid conditions. In the YZK2 and YZK1 boreholes located at the basin margin, a small amount of muddy sandstone is observed. The shale exhibits a deep-gray color, while the gypsum occurs as horizontal layers with developed laminations. This indicates a transition from shallow to deep lake conditions and a decrease in salinity, reflecting deposition in a deep-lake to semi-deep-lake environment.

The upper section of the Dawenkou Formation (FA1) is mainly composed of fine sandstone, shale, and siltstone, which reflects the warm–humid climatic condition. The base of this section exhibits laminations, indicating a shallow water environment. In some parts of the shale, there are visible fragments of biogenic debris and small amounts of interbedded oil shale. This suggests limited deposition in a shallow-water area dominated by algal sedimentation, with a decrease in lake water salinity that is typical of a lacustrine shoreline depositional environment (Figure 6).

### 5.1.2. Trace Element Geochemistry

Trace elements have special geochemical properties that are closely related to their depositional environment, and are usually not affected by anadiagenesis. Thus, analyzing the trace element content and distribution in sedimentary rocks, especially the ratio of some related elements, can infer the depositional environment and geological conditions during the period of formation [43–45]. The ratios of the macronutrient and trace element concentrations, as well as the geochemistry of some elements in sediments, are often used for sedimentary environment discrimination and paleoclimate reconstruction [46,47].

#### Paleosalinity

The ratios of B/Ga, Sr/Ba, and Th/U have been demonstrated to be effective indicators of paleosalinity during the sedimentation process [48–56]. Zhong et al. (2012) proposed a comprehensive indicator for the different types of paleosalinity based on Sr/Ba and B/Ga values: when the B/Ga ratio exceeds six and the Sr/Ba ratio surpasses one, it signifies a saline or ultra-saline water environment. In instances where the B/Ga ratio ranges from greater than two to less than six, and the Sr/Ba ratio falls between 0.5 and 1, it denotes a brackish water environment. Conversely, a B/Ga ratio below two coupled with a Sr/Ba ratio under 0.5 indicates a freshwater environment [55]. However, boron enrichment resulting from volcanic and hydrothermal activities can impact the discrimination of B/Ga in paleosalinity [57]. Since there was no volcanic or hydrothermal activity in the Huanggang Depression during the Paleogene period, boron enrichment is negligible. The Th/U can be used as an index to distinguish marine and terrestrial deposits. Generally, a Th/U greater than seven indicates a terrestrial freshwater environment, two to seven indicates a brackish sedimentary environment, and less than two indicates a marine saline environment [58].

The results from this study show a strong correlation of the B/Ga, Sr/Ba, and Th/U ratios within the Dawenkou Formation (Figure 4 and Table 3). In the lower section, the majority of B/Ga and Sr/Ba ratios fall within the range of freshwater to slightly brackish water (the B/Ga value was 1.28–4.91; the Sr/Ba value was 0.35–0.94; and the Th/U value was 1.74–5.32). These ratios exhibit an increasing trend from deeper to shallower sections. The lithology in this section predominantly consists of purple–red muddy siltstone at the base, transitioning gradually to alternating purple–red and gray–green siltstone towards the top section. Additionally, there is a small amount of hard gypsum present at the uppermost part, indicating the transition of the water body from freshwater to slightly brackish and saline conditions.

The mineral-bearing layers in the middle section of the Dawenkou Formation are characterized by a high salt content. The B/Ga, Sr/Ba, and Th/U ratios in this section

suggest a brackish water to hypersaline water environment (the B/Ga value was 2.29–14.69; the Sr/Ba value was 0.52–34.14; and the Th/U value was 0.52–4.86), with the higher values aligning well with the occurrence of rock salt layers. Notably, the ratios of rock salt are higher in thicker layers compared to thinner layers.

Moving to the upper section, the B/Ga ratio remains within the range of slightly brackish water (2.28–4.72), while the Sr/Ba ratio falls within the range of slightly brackish water to saline water (0.18–5.61) and the Th/U ratio is similar to the situation of Sr/Cu (2.79–5.77). These ratios gradually decrease from deeper to shallower sections, accompanied by lithological changes from mudstone and gypsiferous mudstone at the base to sandstone and mudstone towards the top section. The observed lithological variations and trace element ratios provide insights into the evolution of the salinization and desalinization processes of the water body. Based on these findings, we conclude that the mineral-bearing layers in the middle section of the Dawenkou Formation represent a depositional environment characterized by brackish water to hypersaline water conditions.

#### Paleowater Depth

Previous studies on modern sedimentation have demonstrated that V + Ni + Mn values serve as reliable indicators of paleowater depth [48,50,59,60]. Liu (1986) found that the concentration of V + Ni + Mn gradually increases from fluvial to lacustrine mudstone in the Cretaceous mudstone of the Songliao Basin [59]. Deng et al. (1993) estimate the value of V + Ni + Mn concentration in the fluvial phase as <150 µg/g; in the shallow lacustrine phase as 150–170 µg/g; in the semi-deep-lake phase as 170–190 µg/g; and in the deep-water lake phase as >190 µg/g [60].

In the lower and upper sections of the Dawenkou Formation, the V + Ni + Mn value exceeds 190 µg/g by a significant margin. The average value in the upper section reaches 760.57 µg/g, while the lower section records an average value of 604.41 µg/g. Notably, both sections have a localized layer of well-developed mudstone and hard gypsum rock, suggesting a depositional setting characterized by deep-water fluvio-lacustrine facies. Conversely, the V + Ni + Mn values in the middle section are markedly lower than those of the upper and lower sections. From the 67 samples analyzed, 30 samples have values below 190 µg/g, while 26 samples have values below 170 µg/g. The high values above 190 µg/g are predominantly found in proximity to the upper and lower sections of the formation and matches with the occurrence of mineral-rich rock salt-bearing layers. Notably, no layered texture is observed in this section, and the rock salt inclusions primarily exhibit a chevron crystal morphology (Figure 3g'). Characteristics such as the development of lithofacies, variations in V + Ni + Mn values, and herringbone crystals suggest that the middle section is predominantly associated with relatively shallow water depths within the mineral-bearing layers (Figure 4).

The Al<sub>2</sub>O<sub>3</sub>, K<sub>2</sub>O, TiO<sub>2</sub>, and P<sub>2</sub>O<sub>5</sub> concentrations represent the mud content of the terrestrial detritus, and their values increase with the deepening of the water body [61], consistent trends in the variations in the four major elemental indicators. The high-value interval is in the lower section of the Dawenkou Formation, while relatively higher values are observed in the upper section. On the other hand, the low-value interval is found in the middle section of the formation. These patterns align with the V + Ni + Mn concentration trend and appear to match well with the lithological characteristics. While there is no halite development in the deep-water lower and upper members, the shallow-water middle member features the development of thick, extensive halite deposits.

#### Paleoclimate

Sensitive trace elements (e.g., Ni, Co, Fe, Mn, Mo, Co, and Cu) in argillaceous sediments are important indicators of past climatic and environmental conditions. Changes in their concentrations and ratios can be used to infer climatic conditions, such as the ratios of dry-loving elements (Sr) and moisture-loving elements (Cu) [48,50,62,63]. The Sr/Cu ratio (ranging from 1 to 10) indicates a humid–subtropical climate, while a ratio greater than

10 suggests an arid or semi-arid climate. Fe, V, Cr, Mn, Co, and Ni reasonably concentrate under moist climatic conditions. Conversely, the increase in water alkalinity because of evaporation enables the precipitation of saline minerals under arid climates; consequently, concentrations of Ca, Na, Mg, K, Ba, and Sr are relatively enriched. Regarding the different geochemical behaviors of these two groups, their ratios of  $\Sigma(\text{Fe} + \text{Mn} + \text{Cr} + \text{Ni} + \text{V} + \text{Co})/\Sigma(\text{Ca} + \text{Mg} + \text{Sr} + \text{Ba} + \text{K} + \text{Na})$  (termed as C-value) are considered to be a climate proxy and used broadly for paleoclimate interpretation. Therefore, different scientists have suggested that C-values of 0–0.2, 0.2–0.4, 0.4–0.6, 0.6–0.8, and 0.8–1.0 represent arid, semi-arid, semi-arid to semi-humid, semi-humid, and humid climates, respectively [64–66].

The results from this study show that 19 samples from the lower section of the Dawenkou Formation exhibit Sr/Cu ratios greater than 10, while five samples fall below this threshold. The C-values of the 19 samples range from 0.21 to 0.64, with an average value of 0.32, while five samples fall below this threshold. This indicates a gradual transition in the climate from warm and humid conditions to a drier, semi-arid climate. In the middle section, the Sr/Cu values are consistently greater than 10, with an average value of 350.17, and the majority values of C are notably below 0.2, indicating an arid climate. Similarly, in the upper section, all samples consistently show Sr/Cu ratios greater than 10, with an average value of 53.09. The average C-value is 0.17, with 10 out of 26 values exceeding 0.2. Notably, shallower portions of the section display lower Sr/Cu ratios compared to the deeper portions, signifying a transition from aridity towards more temperate and humid conditions (Figure 4).

Furthermore, it is worth noting that the middle section of the Dawenkou Formation represents a salt-bearing layer, as evidenced by significantly higher Sr/Cu ratios and lower C ratios compared to the upper and lower sections. These results suggest that the Dawenkou Formation was deposited under different climate conditions. The middle member of the formation, which contains thick halite deposits, was deposited in an arid/semi-arid climate environment, while the upper and lower members were deposited under humid–subtropical conditions. The Sr/Cu and C ratios provide valuable information for understanding past climatic trends and their impact on sedimentation processes.

#### Redox Control in Paleoenvironments

The distribution of V and Ni is influenced by oxidation–reduction conditions; thus, their accumulation or depletion in the sedimentary record is useful for tracking redox processes in ancient landscapes. Hatch and Leventhal (1992) compared  $V/(V + \text{Ni})$  ratios to other geochemical redox indicators, and suggested ratios greater than 0.84 for euxinic conditions, 0.54 to 0.82 for anoxic waters, and 0.46–0.60 for dysoxic conditions [50]. Since then, many scholars have adopted this [67–69].

Data from this study show that the  $V/(V + \text{Ni})$  values in the lower and upper sections of the Dawenkou Formation suggest an anaerobic and/or weakly reducing environment. The middle section, comprising a total of 67 samples, has an average  $V/(V + \text{Ni})$  value of 0.64, and ranges from 0.24 to 0.79. These data suggest an oxidizing to weakly reducing environment within the middle section of the Dawenkou Formation (Figure 4).

Uranium (U) is often found in argillaceous rocks and is known for its active properties, ease of oxidation, and leaching loss, indicating a strong migration ability. The  $\delta U$  method is commonly used to determine the oxidation–reduction state of the sedimentary environment, which can be calculated using the formula  $\delta U = U/[0.5 \times (U + \text{Th}/3)]$ . In normal water environments,  $\delta U < 1$ , while in anoxic reduction environments,  $\delta U > 1$  [70–72].

Most of the  $\delta U$  values for the upper and lower members of the Dawenkou Formation are slightly less than one. By contrast, 40 out of the 67 values in the middle member are greater than one (Figure 4). Based on the above two indicators, it can be inferred that the sedimentary environment of the Dawenkou Formation was generally characterized by weak oxidation–reduction conditions.

### 5.1.3. Evolution of the Sedimentary Environment

Based on sedimentological and geochemical indicators, the evolution of the paleolake in the Huanggang Depression from the Eocene to the Oligocene can be divided into six distinct stages. These stages include a cyclical transition from a freshwater lake to a brackish water and then to a saline lake, followed by a transition to a salt lake, and finally back to a freshwater lake. We utilized trace element concentrations and ratios such as B/Ga, Sr/Ba, and V + Ni + Mn to discriminate between these transitional phases (Figure 2).

In the freshwater environment, the dominant lithological assemblage is interbedded mudstone and sandstone, with minerals mainly composed of calcite, illite, feldspar, and quartz. A small number of bioclasts are observed in the mudstone, while layered gypsum is partially present. Evaporation-enriched elements, such as B and Sr, are present in very low concentrations. The transition between freshwater and saline environments is not characterized by abrupt changes, but rather by the presence of transitional brackish water conditions. This is evidenced by elevated levels of B and Sr, as well as an increase in the B/Ga and Sr/Ba ratios. The lithological assemblage primarily consists of thinly layered gypsum, mudstone, and intermittent occurrences of carbonate rocks.

Under saline-lake and salt-lake conditions, the concentrations of B and Sr, as well as the B/Ga and Sr/Ba ratios, significantly increase. The lithofacies assemblages are mainly composed of alternating layers of anhydrite, halite, and a small amount of mudstone, with thin layers of oil shale locally intercalated. This suggests that halite in the Huanggang Depression was primarily developed in a shallow water environment.

### 5.2. Depositional Models

Large salt deposits around the world are mainly located in arid zones within the subtropical high belt, typically between latitudes 15° and 35° in both hemispheres [23,42,73,74]. The location of the subtropical climate zone changes over geological timescales, and during the Eocene and Oligocene, the Huanggang depression was situated within this zone [74–77] (Figure 7). This suggests an alignment between regional and global climate changes. During the early Oligocene, the previously arid climate gradually became cold and dry, leading to strong evaporation, the concentration of water bodies, and the accumulation of salt minerals that formed salt deposits. By the middle Oligocene, the climate had become warm and humid. Sedimentary records and pollen data from the Dawenkou Formation in the Dawenkou Basin, which were contemporaneous with the Huanggang Depression, show a transition from dry and hot to warm and humid conditions during the Eocene and early Oligocene [78].

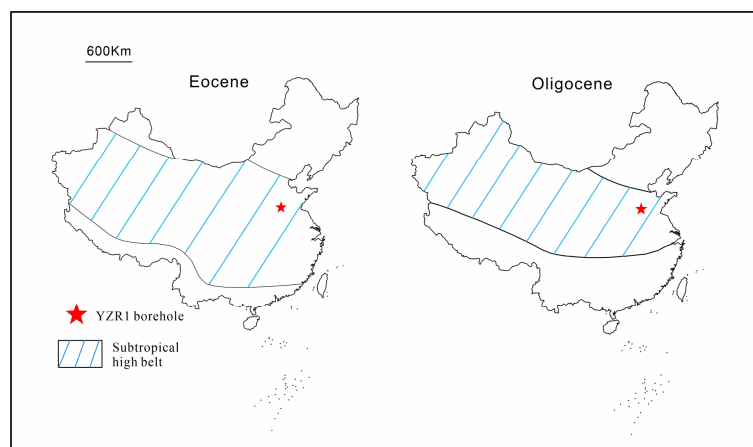


**Figure 7.** Subtropical high-pressure belt in the Eocene and Oligocene (modified from Sun et al., 2005 [77]) and the location of borehole YZR1.

The trace elements and petrographic characteristics of well YZR1 indicate that the paleoclimate was the main control for the halite deposition pattern in the study area

during certain tectonic settings. Two metallogenic models can be proposed based on this observation.

The first model (LA1) infers the metallogenic model of thick rock salt. During slow tectonic subsidence or periods of stable tectonic activity, the paleoclimate plays a major role in mineralization. In continuous drought conditions, when the rate of evaporation exceeds the rate of tectonic subsidence and the lake falls to a shallow water level, brine waters become highly concentrated, and since there is no precipitation at this stage, the brine waters evaporate, which leads to the formation of mineralized salts as residue. Geochemical indicators, such as B/Ga, Sr/Ba, and V + Ni + Mn from trace elements, recorded high values, while the major elements, e.g., Al<sub>2</sub>O<sub>3</sub>, K<sub>2</sub>O, TiO<sub>2</sub>, and P<sub>2</sub>O<sub>5</sub>, have lower values. This overall trend shows a gradual and coherent pattern (Figures 4 and 5). The primary lithological composition of this layer predominantly consists of gray–black rock salt interspersed with blocky gypsum formations. Notably, the fluid inclusions within the rock salt are characterized by “Λ”-shaped crystals, while some hopper crystals have a similar “V” shape (Figure 3g’). Solar radiation and an arid climate are two major reasons for brine concentration, water level reduction, and evaporite deposition [79,80]. However, in arid climate regimes, an insufficient fresh water supply may result in a further decrease in water levels and cause clastic sediments to be loosely packed. As a result, sand silts are carried into shallow lakes by surrounding terrestrial fresh water and wind, promoting desalination and dissolution to some extent. The dissolved salt substances in the brine of the lake basin exhibit a prominent migration pattern from the margin to the center as the lake level gradually decreases. In arid climatic conditions, the rapid rate of evaporation surpasses the replenishment rate of freshwater, resulting in a sustained shallowness of the water body. Consequently, salt substances precipitate and co-deposit with the primary rock salt, forming extensive halite layers of significant thickness (Figure 8a). Freshwater, carrying sediment-laden debris, is introduced into the lake. As the salinity of the water body decreases and salt precipitation ceases, this process triggers the deposition of gypsiferous mudstone and mudstone. The re-deposited rock salt layer exhibits a reduction in primary fluid inclusions. Additionally, certain sections of the white-colored, thick salt layers demonstrate relatively lower densities, suggesting a weakened compaction process during the dissolution and re-deposition phases. This phase roughly corresponds to the low amplitude of the ultra-long eccentricity cycle, indicating a small seasonal variation [27], further supporting the proposed hypothesis.

The second model (LA2) explains the metallogenic model of thin rock salt. During the transitional phase from arid to semi-arid paleoclimates, the periodicity in climatic variations emerged as the major control, leading to the episodic deposition of thin rock salt layers that exhibit a strong correspondence with the minimum values of the short eccentricity cycles [27]. Within this specific layer, trace elements, including B/Ga, Sr/Ba, and V + Ni + Mn, have an overall modest concentration compared to LA1, while the major elements (Al<sub>2</sub>O<sub>3</sub>, K<sub>2</sub>O, TiO<sub>2</sub>, and P<sub>2</sub>O<sub>5</sub>) have a slight increase in their concentrations. Both the trace and major element concentration values display intermittent wave-like patterns. The lithologic composition of this distinct stratigraphic layer primarily consists of alternating rock salt and evaporitic mudstone, occasionally intercalated with minor amounts of shale. Notably, the gypsum formations within this layer predominantly manifest as being thinly bedded with indurated structures. In dry summers and dry/cold winters, the rate of evaporation of the lake exceeds the rate of tectonic subsidence and results in the formation of thin layers of halite at the lake bottom as the water becomes saturated. In contrast, under hot/humid summers and warm winters, the lake water is replenished by atmospheric precipitation and surrounding fresh water, which transports argillaceous sediments to the center of the lake. The evaporation rate of the lake water is close to or less than the sedimentation rate of the lake basin, causing the lake to deepen and gypsiferous mudstone to be deposited at these intervals. During this process, the consolidated halite layers are dissolved by freshwater, resulting in dissolution and recrystallization cycles. During the rapid and repetitive cycles of expansion and contraction of the lake’s surface area, the influx

of terrestrial particles, either transported by the lake shore or wind, becomes a part of the sedimentary material during the crystallization process. Consequently, a portion of the rock salt formations acquires an ashen-black hue, highlighting the dominance of mud-like constituents in the crystallization process (Figure 8b).

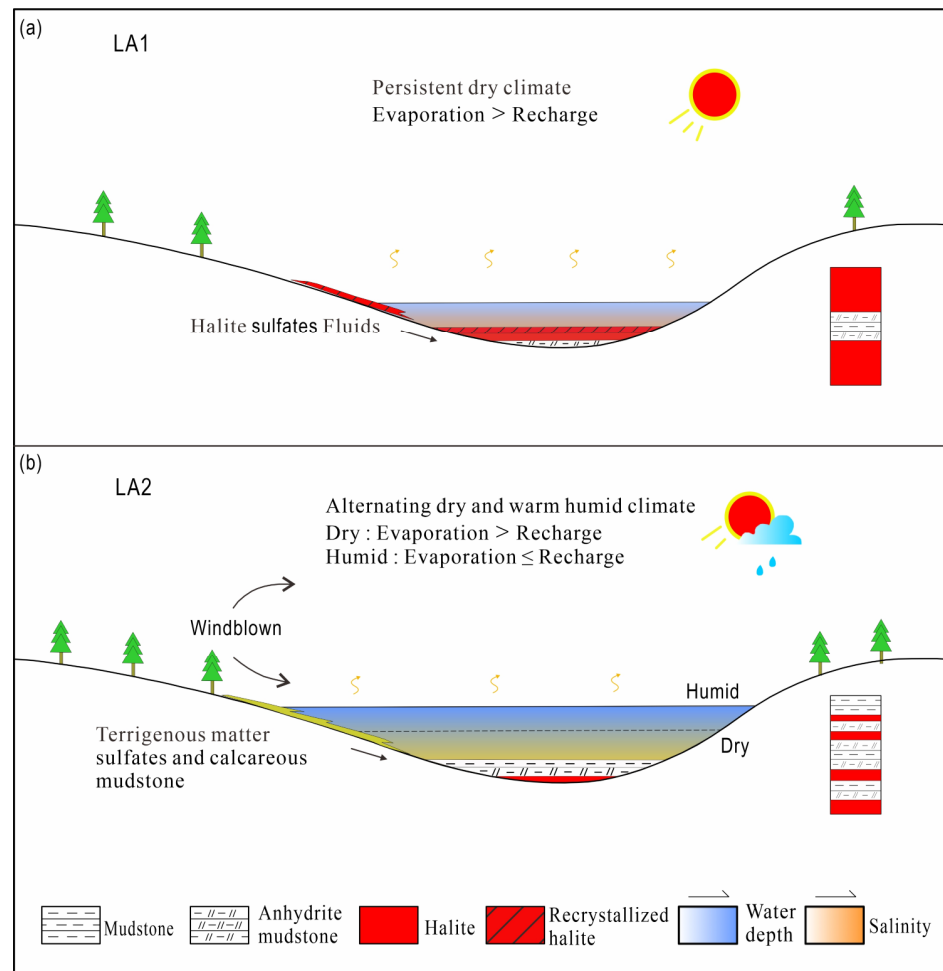


**Figure 8.** Salt formation pattern of the middle member of the Dawenkou Formation in the Huanggang Depression (modified from Ge, 2023, and Bukowski K., 2007 [81,82]) (a) LA1: under arid and semi-arid conditions, the precipitation rate is lower than the evaporation rate; deposition under strong evaporation, high salinity, and disturbed environments. (b) LA2: dry and wet alternating climate, enhanced surface water replenishment, reduced evaporation, lower salinity than LA1, and frequent lake level changes.

Based on the comparison of the different salt-forming models and the comprehensive analyses of the sedimentary record and elemental geochemistry, we suggest that thick halite layers in the Huanggang Depression mainly formed in shallow lake environments under a persistent arid climate, while the thin halite layers formed in shallow lake environments under periodic dry and wet climates.

## 6. Conclusions

During the Paleogene period, massive halite deposits were formed in eastern China. In this study, we conducted a comprehensive analysis of the petrography and primary trace geochemistry of drill core YZR1 in the Huanggang Depression, located in eastern China. Our investigation aimed to provide a preliminary examination of the paleoclimate variations. These are embedded within the thick and thinly layered saline-gypsum mudstone-mudstone lake-phase depositional rhythms documented in the drill cores.

(1) The middle Dawenkou Formation in the Huanggang Depression is characterized by saline-to-hypersaline lake water deposits, which likely formed during arid to semi-arid climatic conditions. Throughout the process of salt-rock formation, the lakes were characterized by relatively shallow water depths, indicative of an overall oxidizing–weakly reducing environment. The geochemical and petrographic analyses from this study show consistent evidence of salinization and desalinization processes in the lake with corresponding changes in the paleoclimate.

(2) The results from this study indicate that the halite deposit in the Huanggang Depression can be explained using two sedimentary models, LA1 and LA2. Thick halite layers formed under the LA1 model through shallow-water evaporation and deposition in a continuously drought-affected environment, while the LA2 model describes an intermittent deposition of thin halite layers due to seasonal periodic changes of dry and wet climates. By comparing the two metallogenic models, we conclude that the thick halite layers in the Huanggang Depression were mainly formed in shallow lake environments under an arid climate, while the thin halite layers were formed in shallow lake environments under periodic changes of dry and wet climates. This study provides a valuable example for understanding Paleogene halite mineralization, shedding light on the paleoclimate and paleoenvironment of the period in eastern China.

**Supplementary Materials:** The following supporting information can be downloaded at: <https://www.mdpi.com/article/10.3390/min14020131/s1>.

**Author Contributions:** Conceptualization, D.L. and W.C.; methodology, W.C. and Z.N.; validation, W.C., D.L. and J.I.E.; formal analysis, B.Y. and C.S.; resources, W.C. and B.Y.; data curation, W.C., C.S. and L.T.; writing—original draft preparation, W.C., D.L. and Z.N.; writing—review and editing, W.C., D.L. and J.I.E.; visualization, W.C. and B.Y.; supervision, Z.Z. and H.J.; project administration, D.L., Z.N. and Z.Z. funding acquisition, W.C. and Z.N. All authors have read and agreed to the published version of the manuscript.

**Funding:** This research was funded by the National Key R&D Plan of China (grant no. 2022YFC2903402), the National Natural Science Foundation of China (grants no. 41772096 and 42102127), the SDUST Research Fund (Grant no. 2018TDJH101), and the Shandong Geological Exploration Fund (2019 no. 6).

**Data Availability Statement:** The original contributions presented in the study are included in the article and Supplementary Materials; further inquiries can be directed to the corresponding authors.

**Acknowledgments:** The sample testing in this study was supported by the Jinan Mineral Resources Supervision and Testing Center, Ministry of Land and Resources.

**Conflicts of Interest:** The authors declare that they have no known competing financial interests or personal relationships that could have appeared to influence the work reported in this paper.

## References

1. Nutting, D.I. Orion of Bedded Salt Deposits: A Critique of Evaporative Models and Defense of a Hydrothermal Model. Ph.D. Thesis, Institute for Creation Research Graduate School, Santee, CA, USA, 1984.
2. Schmalz, R.F. Deep water evaporate deposition: A genetic model. *Ameriean Assoc. Pet. Geol. Bull.* **1969**, *53*, 798–823.
3. Last, W.M. Deep-water evaporite mineral formation in lakes of western Canada. *Spec. Publ.—Soc. Econ. Paleontol. Mineral.* **1994**, *51–58*.
4. Manzi, V.; Lugli, S.; Lucchi, F.R.; Roveri, M. Deep-water clastic evaporites deposition in the Messinian Adriatic foredeep (northern Apennines, Italy): Did the Mediterranean ever dry out? *Sedimentology* **2005**, *52*, 875–902. [[CrossRef](#)]
5. Meilijson, A.; Steinberg, J.; Hilgen, F.; Bialik, O.M.; Waldmann, N.D.; Makovsky, Y. Deep-basin evidence resolves a 50 year old debate and demonstrates synchronous onset of Messinian evaporite deposition in a non-desiccated Mediterranean. *Geology* **2018**, *46*, 243–246. [[CrossRef](#)]
6. Sirota, I.; Enzel, Y.; Lensky, N.G. Halite focusing and amplification of salt layer thickness: From the Dead Sea to deep hypersaline basins. *Geology* **2018**, *46*, 851–854. [[CrossRef](#)]
7. Aloisi, G.; Moneron, J.; Guibourdenche, L.; Camerlenghi, A.; Gavrieli, I.; Bardoux, G.; Agrinier, P.; Gvirtzman, Z. Modes of deep basin halite accumulation during the Messinian Salinity Crisis. In Proceedings of the EGU General Assembly 2023, Vienna, Austria, 24–28 April 2023. No. EGU23-17206.

8. Sirota, I.; Enzel, Y.; Mor, Z.; Ben Moshe, L.; Eyal, H.; Lowenstein, T.K.; Lensky, N.G. Sedimentology and stratigraphy of a modern halite sequence formed under Dead Sea level fall. *Sedimentology* **2021**, *68*, 1069–1090. [[CrossRef](#)]
9. Hardie, L.A.; Eugster, H.P. The depositional environment of marine evaporites: A case for shallow, elastic accumulation. *Sedimentology* **1971**, *16*, 187–220. [[CrossRef](#)]
10. Babel, M. Depositional environments of a salina-type evaporite basin recorded in the Badenian gypsum facies in the northern Carpathian Fore deep. *Geol. Soc. Lond. Spec. Publ.* **2007**, *285*, 107–142. [[CrossRef](#)]
11. Yuan, J.; Huo, C.; Cai, K. The high mountain-deep basin saline environment a new genetic model of salt deposits. *Geol. Rev.* **1983**, *29*, 159–164.
12. Zhang, P. Discussion Oil some geological problems of the research on Evaporite in China. *Acta Sedimentol. Sin.* **1992**, *10*, 78–83.
13. Zheng, M.P.; Chen, W.X.; Qi, W. New Findings and Perspective Analysis of Prospecting for Volcanic Sedimentary Boron Deposits in the Tibetan Plateau. *Acta Geosci. Sin.* **2016**, *37*, 407–418.
14. Roveri, M.; Flecker, R.; Krijgsman, W.; Lofi, J.; Lugli, S.; Manzi, V.; Stoica, M.; Sierro, F.J.; Bertini, A.; Camerlenghi, A.; et al. The Messinian Salinity Crisis: Past and future of a great challenge for marine sciences. *Mar. Geol.* **2014**, *352*, 25–58. [[CrossRef](#)]
15. Gao, H.; Chen, F.; Liu, G.; Liu, Z. Advance problems and prospect in studies of origin of salt rocks of the paleogene Shahejie formation in Dongpu Sag. *J. Palaeogeogr.* **2009**, *11*, 251–261.
16. Jin, Q.; Huang, X. Studies on the origin of the Early Tertiary salt lake Dongpu depression: A postulated deep water model. *J. Univ. Pet. China* **1985**, *10*, 1–13.
17. Gao, H.; Zheng, R.; Xiao, Y.; Meng, F.; Chen, F.; Bai, G.; Luan, Y.; Tan, X.; Shi, Y. Origin of the salt rock of Paleogene Shahejie Formation in Dongpu sag, Bohai Bay Basin: Evidences from sedimentology and geochemistry. *Acta Pet. Sin.* **2015**, *36*, 19–32.
18. Yuan, J.; Zhao, C.; Zhang, S. Genetic model of the deep water salt lake of the Paleogene Sha-4 Member in Dongying sag. *Acta Sedimentol. Sin.* **2000**, *18*, 114–118.
19. Wang, W.; Zhang, M. Study on deep water resedimented origin of saline sediments of E1 f4 in Zhaoji sag, Hongze depression, northern Jianguo Basin. *Acta Sedimentol. Sin.* **2015**, *33*, 242–253.
20. Li, C.; Guo, P.; Liu, C. Deposition models for the widespread Eocene bedded halite in China and their implications for hydrocarbon potential of salt-associated mudstones. *Mar. Pet. Geol.* **2021**, *130*, 105132. [[CrossRef](#)]
21. Ji, Y.; Ren, H.; Zhang, S.; Ma, Z.; Niu, J.; Guo, S.; Gao, C.; Liu, X. Paleogene palaeogeography and oil and gas distribution in Bohai Bay Basin. *J. Palaeogeogr.* **2022**, *24*, 611–633.
22. Tang, L.; Zhang, S.; Yu, X.; Tian, J.; Yang, B.; Luo, W.; Chen, W.; Liang, J.; Ma, X.; Wu, K. Geological characteristics and prospecting potentials of rock salt deposit in Huanggang Subdepression in southwest Shandong Province. *Shandong Land Resour.* **2021**, *37*, 1–10.
23. Zhang, Z.; Zhang, C.; Wang, S.; Liu, S.; Wang, L.; Du, S.; Song, Z.; Zhang, S.; Yang, E.; Cheng, G.; et al. Views on classification and contrast of tectonic units in strata in Shandong Province. *Shandong Land Resour.* **2014**, *30*, 1–23.
24. Liu, Q. *Mesozoic and Cenozoic Terrigenous Clastic-Chemical Rock Salt Deposits in China*; Beijing Science and Technology Press: Beijing, China, 1987; pp. 1–154.
25. Zhu, G.; Jiang, D.; Zhang, B.; Chen, Y. Destruction of the eastern North China Craton in a backarc setting: Evidence from crustal deformation kinematics. *Gondwana Res.* **2012**, *22*, 86–103. [[CrossRef](#)]
26. Zhao, T.; Zhu, G.; Xiang, B.; Lin, S.; Gu, C. Discussion on Initial Mechanism of the Tan-Lu Fault Zone. *Acta Metall. Sin.* **2016**, *35*, 1120–1140.
27. Song, C.; Lv, D.; Chang, J.; Ejembi, J.I.; Tang, L.; Raji, M.; Chen, W.; Zhang, Z. Astronomically forced saline lake deposition and paleoclimatic response in the Huanggang Basin during the Paleogene, Eastern China. *Ore Geol. Rev.* **2023**, *158*, 105506. [[CrossRef](#)]
28. Mjos, R.; Prestholm, E. The geometry and organization of fluviodeltaic channel sandstones in the Jurassic Saltwick Formation, Yorkshire, England. *Sedimentology* **1993**, *40*, 919–935. [[CrossRef](#)]
29. Reading, H.G. (Ed.) *Sedimentary Environments: Processes, Facies and Stratigraphy*; John Wiley & Sons: Hoboken, NJ, USA, 2009.
30. Miall, A.D. *The Geology of Fluvial Deposits: Sedimentary Facies, Basin Analysis, and Petroleum Geology*; Springer: Berlin/Heidelberg, Germany, 2013.
31. Ortí, F.; Salvany, J.M. Coastal salina evaporites of the Triassic-Liassic boundary in the Iberian Peninsula: The Alacón borehole. *Geol. Acta* **2004**, *2*, 291–304.
32. Ortí, F.; Rosell, L.; Anadón, P. Deep to shallow lacustrine evapo-rites in the Libros Gypsum (Southern Teruel Basin, Miocene, NE Spain): An occurrence of pelletal gypsum rhythmites. *Sedimentology* **2003**, *50*, 361–386. [[CrossRef](#)]
33. Warren, J.K. *Evaporites: A Geological Compendium*, 2nd ed.; Springer: Cham, Switzerland, 2016.
34. Garber, R.A.; Levy, Y.; Friedman, G.M. The sedimentology of the Dead Sea. *Carbonates Evaporites* **1987**, *2*, 43–57. [[CrossRef](#)]
35. Roedder, E. Volume 12: Fluid inclusions. *Mineral. Soc. Am.* **1984**, *12*, 644.
36. Handford, C. Halite depositional facies in a solar salt pond: A key to interpreting physical energy and water depth in ancient deposits? *Geology* **1990**, *18*, 691–694. [[CrossRef](#)]
37. Zambito, J.J., IV; Benison, K.C. Extremely high temperatures and paleoclimate trends recorded in Permian ephemeral lake halite. *Geology* **2013**, *41*, 587–590. [[CrossRef](#)]
38. Zhou, Z.; Dong, Q.; Hou, G.; Xu, C.; Miao, C. The forming environment and sedimentary evolution of the oil shale intergrowing with salt alkali mine-with the oil shale deposit of Wucheng, Tongbai Basin as an example. *J. Jilin Univ. (Earth Sci. Ed.)* **2006**, *36*, 1001–1005.

39. Eugster, H.P.; Surdam, R.C. Depositional environment of the Green River Formation of Wyoming: A preliminary report. *Geol. Soc. Am. Bull.* **1973**, *84*, 1115–1120. [[CrossRef](#)]
40. Cohen, P.A.; Macdonald, F.A.; Pruss, S.; Matys, E.; Bosak, T. Fossils of putative marine algae from the Cryogenian glacial interlude of Mongolia. *Palaios* **2015**, *30*, 238–247. [[CrossRef](#)]
41. Warren, J.K. Evaporites through time: Tectonic, climatic and eustatic controls in marine and nonmarine deposits. *Earth-Sci. Rev.* **2010**, *98*, 217–268. [[CrossRef](#)]
42. Bechtel, A.; Jia, J.; Strobl, S.A.; Sachsenhofer, R.F.; Liu, Z.; Gratzner, R.; Püttmann, W. Palaeoenvironmental conditions during deposition of the Upper Cretaceous oil shale sequences in the Songliao Basin (NE China): Implications from geochemical analysis. *Org. Geochem.* **2012**, *46*, 76–95. [[CrossRef](#)]
43. Xu, Z.; Wang, Z.; Hu, S.; Zhu, S.; Jiang, Q. Paleoclimate During Depositional Period of the Upper Triassic Xujiahe Formation in Sichuan Basin. *J. Palaeogeogr.* **2010**, *12*, 415–424.
44. Wang, K.; Luo, S. Geochemical characters of carbonates and indicative significance of sedimentary environment: An example from the Gaoyuzhuang formation of the Changcheng system in the northern Hebei Depression. *Oil Gas Geol.* **2009**, *30*, 343–349.
45. Hu, M. Analyzing sedimentary environment using geochemical indicators—An example from north margin of Middle Yantze platform in Last Sinian. *Pet. Explor. Dev.* **1999**, *26*, 39–41.
46. Song, C. Late Cenozoic Element Characters and Palaeoclimatic Change of the Lacustrine Sediments in Linxia Basin, China. *Acta Sedimentol. Sin.* **2007**, *25*, 409–416.
47. Li, M.; Kang, S. Responses of lake sediments to palaeoenvironmental and palaeoclimatic changes in Tibetan Plateau. *J. Salt Lake Res.* **2007**, *15*, 63–72.
48. Dill, H. Metallogenesis of early Paleozoic graptolite shales from the Graefenthal Horst (Northern Bavaria-Federal Republic of Germany). *Econ. Geol.* **1986**, *81*, 889–903. [[CrossRef](#)]
49. Li, C.; Xiao, J. The application of trace element to the study on paleosalinities in Shahejie Formation of Dongying Basin Shengli oilfield. *Acta Sedimentol. Sin.* **1988**, *6*, 100–107.
50. Hatch, J.R.; Leventhal, J.S. Relationship between inferred redox potential of the depositional environment and geochemistry of the Upper Pennsylvanian (Missourian) Stark Shale Member of the Dennis Limestone, Wabaunsee County, Kansas, USA. *Chem. Geol.* **1992**, *99*, 65–82. [[CrossRef](#)]
51. Sun, Z. *Sedimentary Environment and Oil and Gas Generation of Cenozoic Salt Lake in China*; Petroleum Industry Press: Beijing, China, 1997; pp. 79–84.
52. Zheng, R.; Liu, M. Study on palaeosalinity of Chang6 oil reservoir set in Ordos basin. *Oil Gas Geol.* **1999**, *20*, 20–25.
53. Shi, Z.; Chen, K.; Shi, J.; Liu, B.; He, H.; Liu, G. Feasibility analysis of the application of the ratio of Strontium to Barium on the identifying sedimentary environment. *Fault-Block Oil Gas Field* **2003**, *10*, 12–16.
54. Song, M. Sedimentary environment geochemistry in the Shasi section of southern ramp, Dongying depression. *Miner. Pet.* **2005**, *25*, 67–73.
55. Zhong, H.; Pu, R.; Yan, H.; Zhao, M.; Xu, J. Analysis on paleosalinity and paleoenvironment of Late Paleozoic in Tarim Basin. *J. Northwest Univ. (Nat. Sci. Ed.)* **2012**, *42*, 74–81.
56. Wei, W.; Algeo, T.J. Elemental proxies for paleosalinity analysis of ancient shales and mudrocks. *Geochim. Cosmochim. Acta* **2020**, *287*, 341–366. [[CrossRef](#)]
57. Dai, S.; Ren, D.; Zhou, Y.; Chou, C.; Wang, X.; Zhao, L.; Zhu, X. Mineralogy and geochemistry of a superhigh-organic-sulfur coal, Yanshan Coalfield, Yunnan, China: Evidence for a volcanic ash component and influence by submarine exhalation. *Chem. Geol.* **2008**, *255*, 182–194. [[CrossRef](#)]
58. Fu, J.; Li, S.; Xu, L.; Niu, X. Paleo-sedimentary environmental restoration and its significance of Chang 7 Member of Triassic Yanchang Formation in Ordos Basin, NW China. *Pet. Explor. Dev.* **2018**, *45*, 998–1008. [[CrossRef](#)]
59. Liu, P.; Zhou, H.; Kang, G. Distribution of elements and its relation with sedimentary environment in Songliao basin. *Daqing Pet. Geol. Dev.* **1986**, *5*, 11–15.
60. Deng, H.; Qian, K. *Sedimentary Geochemistry and Environment Analysis*; Gansu Science and Technology Press: Lanzhou, China, 1993; pp. 95–104.
61. Mao, X.; Zhou, L.; Yang, F.; Pu, L. Geochemical characteristics and its sedimentary environment significance of the Ordovician in the southwestern margin of Ordos basin. *Geol. Sci. Technol. Inf.* **2011**, *30*, 98–102.
62. Fan, Y.; Qu, H.; Wang, H.; Yang, X.; Feng, Y. The application of trace elements analysis to identifying sedimentary media environment: A case study of Late Triassic strata in the middle part of western Ordos Basin. *Geol. China* **2012**, *39*, 382–389.
63. Jin, M.; Li, W. Petrogeochemical characteristics of Lower Cretaceous and Pliocene rocks and paleoclimate evolution in Wulanhuaregion. *Uranium Geol.* **2003**, *19*, 349–354.
64. Zhao, Z.Y.; Zhao, J.H.; Wang, H.J.; Liao, J.D.; Liu, C.M. Distribution characteristics and applications of trace elements in Junggar Basin. *Nat. Gas Explor. Dev.* **2007**, *30*, 30–33.
65. Cao, J.; Wu, M.; Chen, Y.; Hu, K.; Bian, L.Z.; Wang, L.G.; Zhang, Y. Trace and rare earth element geochemistry of Jurassic mudstones in the northern Qaidam Basin, northwest China. *Geochemistry* **2012**, *72*, 245–252. [[CrossRef](#)]
66. Fu, X.; Wang, J.; Chen, W.; Feng, X.; Wang, D.; Song, C.; Zeng, S. Elemental geochemistry of the early Jurassic black shales in the Qiangtang Basin, eastern Tethys: Constraints for palaeoenvironment conditions. *Geol. J.* **2016**, *51*, 443–454. [[CrossRef](#)]
67. Wignall, P.B. *Black Shales*; Clarendon Press: Oxford, UK, 1994; p. 46.

68. Xiong, G.; Wang, J.; Hu, R. Trace element characteristics and sedimentary environment of the Sinian system of the Fanjingshan area in Guizhou province. *Acta Geosci. Sin.* **2008**, *29*, 51.
69. Rimmer, S.M. Geochemical paleoredox indicators in Devonian–Mississippian black shales, central Appalachian Basin (USA). *Chem. Geol.* **2004**, *206*, 373–391. [[CrossRef](#)]
70. Jones, B.; Manning, D.A.C. Comparison of geochemical indices used for the interpretation of palaeoredox conditions in ancient mudstone. *Chem. Geol.* **1994**, *111*, 111–129. [[CrossRef](#)]
71. Wignall, P.B.; Twitchett, R.J. Oceanic anoxia and the end Permian mass extinction. *Science* **1996**, *272*, 1155–1158. [[CrossRef](#)]
72. Liu, A.; Li, X.; Wang, C.; Wei, K.; Wang, B. Analysis of geochemical feature and sediment environment for hydrocarbon source rocks of Cambrian in west Hunan-Hubei area. *Acta Sedimentol. Sin.* **2013**, *31*, 1122–1132.
73. Cung, T.C.; Geissman, J.W. A review of the paleomagnetic data from Cretaceous to Lower Tertiary rocks from Vietnam, Indochina and South China, and their implications for Cenozoic tectonism in Vietnam and Adjacent areas. *J. Geodyn.* **2013**, *69*, 54–64. [[CrossRef](#)]
74. Akhmetiev, M.A. Paleocene and Eocene floristic and climatic change in Russia and northern Kazakhstan. *Bull. Geosci.* **2010**, *85*, 77–94. [[CrossRef](#)]
75. Chen, H.; Xie, X.; Van Rooij, D.; Vabdorpe, T.; Su, M.; Wang, D. Depositional characteristics and processes of alongslope currents related to a seamount on the northwestern margin of the Northwest Sub-Basin, South China Sea. *Mar. Geol.* **2014**, *355*, 36–53. [[CrossRef](#)]
76. Quan, C.; Liu, Z.; Utescher, T.; Jin, J.; Shu, J.; Li, Y.; Liu, Y. Revisiting the Paleogene climate pattern of East Asia: A synthetic review. *Earth-Sci. Rev.* **2014**, *139*, 213–230. [[CrossRef](#)]
77. Sun, X.; Wang, P. How old is the Asian monsoon system?—Palaeobotanical records from China. *Palaeogeogr. Palaeoclimatol. Palaeoecol.* **2005**, *222*, 181–222. [[CrossRef](#)]
78. Zhu, M. Study on the origin of salt deposit in Dawenkou Basin in Shandong province. *Shandong Land Resour.* **2015**, *31*, 27–30.
79. Chen, Y.; Wang, Y.; Guo, M.; Wu, H.; Li, J.; Wu, W.; Zhao, J. Differential enrichment mechanism of organic matters in the marine-continental transitional shale in northeastern Ordos Basin, China: Control of sedimentary environments. *J. Nat. Gas Sci. Eng.* **2020**, *83*, 1875–5100. [[CrossRef](#)]
80. Liu, W.; Yao, J.; Tong, N.; Qiao, Y.; Chen, Y. Organic matter accumulation on the Dalong Formation (Upper Permian) in western Hubei, South China: Constraints from multiple geochemical proxies and pyrite morphology. *Palaeogeogr. Palaeoclimatol.* **2019**, *514*, 677–689. [[CrossRef](#)]
81. Ge, T.; Jiang, Z.; Kong, X.; Bao, H.; Chen, F.; Wu, S.; Guo, L.; Yang, Y.; Liu, T.; Zhang, J. Salt rhythmite formation and organic matter enrichment in the Qianjiang formation, Jiangnan Basin, China: Constraints from alternating dry and wet climates. *Mar. Pet. Geol.* **2023**, *148*, 106067. [[CrossRef](#)]
82. Bukowski, K.; Czapowski, G.; Karoli, S.; Babel, M. Sedimentology and geochemistry of the Middle Miocene (Badenian) salt-bearing succession from East Slovakian Basin (Zbudza Formation). In *Evaporites Through Space and Time*; Schreiber, B.C., Lugli, S., Babel, M., Eds.; Geological Society, Special Publications: London, UK, 2007; Volume 285, pp. 247–264.

**Disclaimer/Publisher’s Note:** The statements, opinions and data contained in all publications are solely those of the individual author(s) and contributor(s) and not of MDPI and/or the editor(s). MDPI and/or the editor(s) disclaim responsibility for any injury to people or property resulting from any ideas, methods, instructions or products referred to in the content.